Computers and Geotechnics 197 (2026) 108165

Contents lists available at ScienceDirect

Computers and Geotechnics

journal homepage: www.elsevier.com/locate/compgeo

Research paper

Interface-enriched generalized finite element method for the coupled hydro-mechanical analysis of piecewise homogeneous porous media

Pouriya Pirmoradi [a], Alejandro M. Aragón [b,*], Payam Poorsolhjouy [a], Akke S.J. Suiker [a,*]

[a] Department of the Built Environment, Eindhoven University of Technology, De Groene Loper 6, 5612 AP Eindhoven, the Netherlands
[b] Faculty of Mechanical Engineering, Delft University of Technology, Mekelweg 2, 2628 CD Delft, the Netherlands

ARTICLE INFO

Keywords:
Interface-enriched generalized finite element method (IGFEM)
Porous media
Weak discontinuity
Material interfaces
Coupled physical phenomena
Monolithic update scheme

ABSTRACT

An Interface-enriched Generalized Finite Element Method (IGFEM) is proposed for the coupled hydro-mechanical analysis of deformable, saturated porous media consisting of distinct, perfectly bonded material phases. The spatial discretization of the momentum balance equation and storage equation is derived using IGFEM, followed by the time discretization of these equations via the generalized Newmark method. This leads to a fully coupled system of nonlinear equations, which is solved iteratively using a monolithic update scheme. The IGFEM formulation is proficient in accurately capturing weak discontinuities in both the solid phase displacement field and the fluid phase pressure field at material interfaces, by placing enriched nodes directly on these interfaces. Several numerical examples demonstrate that the proposed IGFEM formulation not only matches the accuracy of standard FEM with a conformal mesh, but also outperforms the eXtended/Generalized Finite Element Method (XFEM/GFEM). Moreover, it can accurately capture complex, non-planar interfaces without requiring mesh alignment, highlighting the method's flexibility and robustness for practical hydro-mechanical analyses of porous media with geometrically intricate boundaries. Overall, IGFEM provides a highly accurate and efficient approach for solving transient coupled problems involving material interfaces.

1. Introduction

The hydro-mechanical behavior of porous media is governed by the interaction between the fluid and solid phases. Accurate prediction of this behavior requires the modeling of the strong coupling between fluid flow and deformation of the solid matrix. The foundational equations describing the quasi-static interaction between the solid skeleton and pore fluid were first introduced by Biot (1941), who later extended the framework to account for dynamic wave propagation (Biot, 1956, 1962). The classical mixture theory, which forms a cornerstone of continuum mechanics for modeling the distinct phases in porous media, was initially formulated by Truesdell and Toupin (1960) and is based on the concept of volume fractions. This theory was further advanced through several key developments: Green and Naghdi (1969) developed a thermodynamically consistent framework that adheres to the second law of thermodynamics; Bowen (1980, 1982) focused on the formulation of rigorous balance laws and interaction forces for both compressible and incompressible porous media; Whitaker (1977) introduced volume averaging techniques to enable micro-to-macro upscaling, and Hassanizadeh and Gray (1980, 1990) extended the framework to address nonequilibrium thermodynamics in the context of multiphase flow and interfacial phenomena. For nonlinear problems involving geometrical and material nonlinearities, iterative solution procedures within the framework of the finite element method (FEM) were advanced by Zienkiewicz et al. (1980), Zienkiewicz (1982), Zienkiewicz et al. (1990a), Prévost (1980), Prevost (1982). Building on these seminal works, numerous numerical models have been developed for the hydro-mechanical analysis of both saturated porous media (Zienkiewicz et al., 1990a; Schrefler et al., 1998; Li et al., 2004; Zhang et al., 2009; Hajiabadi and Khoei, 2019; Scheperboer et al., 2022) and partially saturated porous media (Zienkiewicz et al., 1990b; Schrefler and Xiaoyong, 1993; Schrefler and Scotta, 2001; Sheng et al., 2003, 2008; Hoteit and Firoozabadi, 2008; Wang et al., 2009; Khoei and Mohammadnejad, 2011; Khoei and Saeedmonir, 2021). A comprehensive overview of the various theoretical frameworks for porous media can be found in the review by De Boer (2012).

Discontinuities in porous media, such as material interfaces, voids, and fractures, significantly influence both the deformation behavior of the solid matrix and the flow pattern of the pore fluid. Consequently, it is essential to accurately account for these features in hydro-mechanical analyses. The finite element method enables the modeling of discontinuous porous media by employing meshes that conform to the geometry

* Corresponding authors.
E-mail addresses: a.m.aragon@tudelft.nl (A.M. Aragón), a.s.j.suiker@tue.nl (A.S.J. Suiker).

https://doi.org/10.1016/j.compgeo.2026.108165
Received 20 December 2025; Received in revised form 22 March 2026; Accepted 14 April 2026
Available online 7 May 2026

of the discontinuities, aligning element edges with fracture or interface locations. This mesh-fitting approach allows for the incorporation of cohesive interface elements, such that the intact regions of the porous medium are modeled using standard finite elements, while fractures are explicitly captured through cohesive elements (Segura and Carol, 2008; Khoei et al., 2011; Sarris and Papanastasiou, 2012; Carrier and Granet, 2012). However, when discontinuities evolve, such as during fracture propagation, this method necessitates mesh adaptivity (Karimi-Fard and Firoozabadi, 2001; Simoni and Secchi, 2003; Monteagudo and Firoozabadi, 2004; Secchi et al., 2007), which can lead to considerable computational inefficiencies.

Enriched finite element methods (*e*-FEMs) have been developed to address the mesh-dependency limitations of traditional FEM by decoupling the finite element discretization from discontinuities. Among these methods, the eXtended Finite Element Method (XFEM) and the Generalized Finite Element Method (GFEM) enable the modeling of both strong and weak discontinuities, i.e., discontinuities in the primary field variables and their spatial gradients, by augmenting the standard finite element function space with additional enrichment functions (Belytschko and Black, 1999; Moës et al., 1999; Daux et al., 2000; Fries and Belytschko, 2010). These enrichment functions allow for adequate resolution of the non-smooth behavior associated with discontinuities, thereby recovering the accuracy typically lost when the mesh is not aligned with the discontinuities. Comprehensive reviews of the theoretical foundations, methodology, and applications of XFEM/GFEM are provided by Khoei (2014) and Aragón and Duarte (2023). Furthermore, a comparative study of fluid flow in fractured or fracturing porous media using XFEM/GFEM and interface elements is presented by de Borst (2017b,a).

Over the past two decades, the application of XFEM/GFEM has become well established in the numerical analysis of pore fluid flow within saturated and partially saturated porous media. Key applications include hydro-mechanical simulations of porous media with material interfaces (Khoei and Haghighat, 2011; Mohammadnejad and Khoei, 2013a), fractured or fracturing porous media (Réthoré et al., 2007, 2008; Callari et al., 2010; Mohammadnejad and Khoei, 2013c; Khoei et al., 2023b,a), and hydraulic fracture propagation (Gordeliy and Peirce, 2013a,b; Remij et al., 2015; Mohammadnejad and Khoei, 2013b; Mohammadnejad and Andrade, 2016; Khoei et al., 2018; Iranmanesh and Pak, 2023). Additional studies have applied XFEM/GFEM to model fluid flow in fractured porous media undergoing large deformations (Irzal et al., 2013), to simulate thermo-hydro-mechanical (THM) coupling in fractured and fracturing domains (Khoei et al., 2012; Varnosfaderani et al., 2017; Iranmanesh and Pak, 2018; Khoei and Mortazavi, 2020; Khoei et al., 2021; Mortazavi and Khoei, 2024), to analyze hot water flooding in naturally fractured oil reservoirs (Mortazavi et al., 2022), and to investigate heat extraction processes in enhanced geothermal systems (Li et al., 2021; Mortazavi et al., 2023).

A distinct class of *e*-FEMs has emerged to address discontinuities by placing enriched nodes directly along interfaces, in contrast to the standard XFEM/GFEM approach, where enrichments are applied to the existing element nodes. These so-called *discontinuity-enriched formulations*, which can be regarded as derivatives of XFEM/GFEM (Aragón and Duarte, 2023), decouple the mesh from discontinuities while recovering several features of standard FEM that are typically lost in XFEM/GFEM. More specifically, because the enrichment functions are nonzero only in cut elements by construction, discontinuity-enriched formulations offer the following key advantages: (i) *Preservation of the Kronecker-δ property of standard shape functions*: Since the enrichment functions vanish at the locations of standard element nodes, the numerical solution matches the nodal values exactly, ensuring that the degrees of freedom (DOFs) associated with standard element nodes retain their physical meaning; (ii) *Simplified enforcement of essential boundary conditions*: Nonzero Dirichlet boundary conditions can be applied as straightforwardly as in standard FEM (Soghrati et al., 2012), including on immersed Dirichlet boundaries, where they can be imposed either weakly (Cuba-Ramos et al., 2015) or strongly (van den Boom et al., 2019); (iii) *Recovery of smooth reactive tractions*: Tractions recovered from Dirichlet boundaries can be accurately retrieved (van den Boom et al., 2019), which addresses a long-standing challenge in XFEM/GFEM (where it is not possible even with stabilization techniques (Haslinger and Renard, 2009)); (iv) *No degraded accuracy in blending elements*: By construction, enrichment functions are exactly zero in *blending elements*—i.e., those adjacent to cut elements—thereby discarding the need of special techniques in XFEM/GFEM to avoid parasitic terms that yield lower accuracy with certain choices of enrichment functions (van den Boom et al., 2021; van Bergen et al., 2024); (v) *Intrinsic numerical stability*: The condition number of the global stiffness matrix, which is a critical factor influencing the stability and efficiency of numerical solvers, scales as $\mathcal{O}\left(h^{-2}\right)$, where h denotes the mesh element size. This scaling is consistent with that of standard FEM using fitted (or geometry-conforming) meshes, and is achieved either by scaling the enrichment functions so that their contribution diminishes near standard nodes, or by applying a simple Jacobi-like diagonal preconditioner (Aragón et al., 2020); and (vi) *Ease of implementation*: Discontinuity-enriched methods are computationally efficient and straightforward to implement, as they allow for the reuse of standard data structures typically employed in displacement-based FEM codes.

Building on the above advantages, within the class of discontinuity-enriched formulations, the Interface-enriched Generalized Finite Element Method (IGFEM) was introduced to handle problems with weak discontinuities (Soghrati et al., 2012; Cuba-Ramos et al., 2015; van den Boom et al., 2019; Aragón et al., 2020). IGFEM has demonstrated optimal convergence for smooth problems without singularities in various studies (Soghrati et al., 2012; Cuba-Ramos et al., 2015; van den Boom et al., 2019; De Lazzari et al., 2021), and its capability in handling more complex scenarios involving material junctions with singularities has been investigated in recent work (Liu et al., 2025). The method was further extended to the Hierarchical Interface-enriched Finite Element Method (HIFEM) (Soghrati, 2014; Aragón et al., 2020), to handle cases where multiple discontinuities cut a single element. It also evolved into the Discontinuity-Enriched Finite Element Method (DE-FEM) (Aragón and Simone, 2017; Zhang et al., 2019; Liu et al., 2025; Zhang et al., 2025), whereby both weak and strong discontinuities are captured via a single three-term enriched approximation. Discontinuity-enriched finite element methods have been applied to a wide range of problems in continuum mechanics, including the analysis of multiphase material systems (Soghrati et al., 2012; Aragón et al., 2013; Soghrati, 2014; Aragón et al., 2020), immersed boundary (fictitious domain) problems (Cuba-Ramos et al., 2015; van den Boom et al., 2019), fracture mechanics problems (Aragón and Simone, 2017; van den Boom et al., 2019; Zhang et al., 2019; De Lazzari et al., 2021; Liu et al., 2025; Zhang et al., 2025), nonconforming mesh coupling and contact problems (Liu et al., 2022), and topology optimization problems (van den Boom et al., 2021; van Bergen et al., 2024; van den Boom et al., 2023; Zhang et al., 2022). However, the applicability of this approach for the analysis of combined physical phenomena involving strongly coupled partial differential equations remains an area yet to be explored.

In this paper, we introduce a novel IGFEM framework for the coupled hydro-mechanical analysis of piecewise homogeneous porous media. Material interfaces in saturated porous media induce discontinuities in the gradients of both the solid displacement and pore-pressure fields, commonly referred to as weak discontinuities. Unlike standard FEM, which requires meshes aligned with material interfaces, IGFEM allows interfaces to cut arbitrarily through elements while accurately capturing these gradient discontinuities in both solid displacement and fluid pressure fields. This hierarchical enrichment in cut elements represents the key innovation of the method, enabling accurate modeling of curved, geometry non-conforming, or otherwise irregular material interfaces without remeshing. The governing equations, which include

the linear momentum balance and the storage equation, are discretized using IGFEM function spaces, and time integration is performed via the Newmark method, resulting in a fully coupled nonlinear system solved monolithically with a Newton–Raphson scheme. The approach is demonstrated on four practical problems: (i) one-dimensional consolidation of a layered soil column, (ii) two-dimensional consolidation of a horizontally stratified soil structure, (iii) water injection into a layered underground reservoir, and (iv) transient response of a horizontally layered soil with a sinusoidal material interface. All IGFEM results are compared with standard FEM using fitted meshes to highlight the method's accuracy and robustness, and the first example is further validated against published XFEM/GFEM results. These demonstrations confirm that IGFEM provides a novel, efficient, and flexible framework for hydro-mechanical problems involving weak discontinuities across material interfaces.

2. Model formulation and enriched finite element discretization

The saturated porous media considered in this study are characterized by a solid matrix with interconnected pores filled with a migrating fluid, which, for instance, can be a gas, water or oil. In the model formulation, it is assumed that the porous medium is subjected to isothermal conditions, and that no mass transfer or chemical reactions occur between the solid matrix and the fluid phase. The governing equations and boundary conditions of the hydro-mechanical problem are introduced in Section 2.1, followed by the weak formulation of the problem in Section 2.2. Section 2.3 presents the spatial discretization using IGFEM. The monolithic update scheme for the temporal integration of the resulting coupled system of algebraic equations is detailed in Section 2.4.

2.1. Governing equations and boundary conditions

The hydro-mechanical behavior of a saturated porous medium is governed by the interactions between its solid and fluid phases. To understand these interactions, it is essential to decompose the total stress $\boldsymbol{\sigma}$ at a material point as follows (Zienkiewicz et al., 1999):

$$\boldsymbol{\sigma} = \boldsymbol{\sigma}' - \alpha p \boldsymbol{I}, \tag{1}$$

where $p = p(\boldsymbol{x}, t)$ is the pressure in the fluid phase, $\boldsymbol{\sigma}' = \boldsymbol{\sigma}'(\boldsymbol{x}, t)$ is the effective stress in the porous skeleton, $\boldsymbol{I}$ is the second-order identity tensor, and α is Biot's coefficient, with $\boldsymbol{x}$ and t the spatial and time coordinates, respectively. Note that in Eq. (1) a negative sign is used for p, since the fluid pressure is generally defined as positive, while, in accordance with the solid mechanics convention, the total stress $\boldsymbol{\sigma}$ (as well as the effective stress $\boldsymbol{\sigma}'$) is positive in tension and negative in compression. Furthermore, Biot's coefficient is defined by $\alpha = 1 - K_t/K_s$, where K_t is the bulk modulus of the porous skeleton and K_s is the bulk modulus of the solid phase composing the porous skeleton. For most soils, the bulk modulus of individual soil particles is much larger than that of the total particle skeleton, so that Biot's coefficient is close to unity; conversely, for rock and concrete the value of α typically ranges between 1/3 and 2/3 (Zienkiewicz et al., 1999).

The hydro-mechanical response of the porous medium is described within the small deformation framework, assuming that the constitutive response of the porous skeleton is elastic, i.e.,

$$\boldsymbol{\sigma}' = \boldsymbol{D}\boldsymbol{\epsilon}, \tag{2}$$

with $\boldsymbol{D}$ the fourth-order elastic stiffness tensor, and $\boldsymbol{\epsilon} = \boldsymbol{\epsilon}(\boldsymbol{x}, t)$ the infinitesimal strain tensor, defined as the symmetric part of the displacement gradient, $\boldsymbol{\epsilon} = \frac{1}{2}\left(\boldsymbol{\nabla u} + (\boldsymbol{\nabla u})^{\top}\right)$, where $\boldsymbol{u} = \boldsymbol{u}(\boldsymbol{x}, t)$ is the displacement of the solid matrix and $\boldsymbol{\nabla}$ is the gradient operator.

For a material point in the saturated porous medium, the overall balance of linear momentum of the solid–fluid mixture is expressed by (Zienkiewicz et al., 1999)

$$\boldsymbol{\nabla}\cdot\boldsymbol{\sigma} - \rho\ddot{\boldsymbol{u}} - \rho_f\left(\dot{\boldsymbol{w}} + (\boldsymbol{\nabla w})\,\boldsymbol{w}\right) + \rho\boldsymbol{b} = \boldsymbol{0}. \tag{3}$$

Here, $\ddot{\boldsymbol{u}} = \ddot{\boldsymbol{u}}(\boldsymbol{x}, t)$ is the acceleration of the solid matrix and $\boldsymbol{w}(\boldsymbol{x}, t)$ is the Darcy velocity, defined as the relative velocity of the fluid with respect to the solid matrix, multiplied by the porosity of the porous medium. Moreover, $\dot{\boldsymbol{w}} = \dot{\boldsymbol{w}}(\boldsymbol{x}, t)$ is the relative acceleration of the fluid phase, which follows from the Darcy velocity as the time derivative with respect to the frame of reference attached to the solid matrix, $\dot{\boldsymbol{w}} = \mathrm{d}\boldsymbol{w}/\mathrm{d}t$. Further, $\boldsymbol{b}$ is the body force (per unit mass), and ρ_f and ρ are the densities of the fluid phase and the porous medium, respectively. The density of the saturated porous medium reads $\rho = n\rho_f + (1-n)\rho_s$, with ρ_s the density of the solid phase and n the porosity, expressed as the ratio between the pore volume and the total volume of the porous medium.

Additionally, the balance of linear momentum of the fluid phase, defined with respect to a reference system attached to the solid matrix, reads (Zienkiewicz et al., 1999)

$$-\boldsymbol{\nabla}p - \boldsymbol{R} - \rho_f\ddot{\boldsymbol{u}} - \frac{\rho_f}{n}\left(\dot{\boldsymbol{w}} + (\boldsymbol{\nabla w})\,\boldsymbol{w}\right) + \rho_f\boldsymbol{b} = \boldsymbol{0}, \tag{4}$$

where $\boldsymbol{R}$ is the viscous drag force (per unit volume). The viscous drag force is determined from Darcy's seepage law, $\boldsymbol{R} = \boldsymbol{w}/k$, with the (isotropic) permeability given by $k = \kappa/\mu$, in which κ is the intrinsic permeability of the porous medium and μ is the dynamic viscosity of the fluid phase.

Further, from the conservation of mass of the solid and fluid phases, the so-called storage equation of the saturated porous medium can be derived as (Zienkiewicz et al., 1999):

$$\boldsymbol{\nabla}\cdot\boldsymbol{w} + \alpha\boldsymbol{\nabla}\cdot\dot{\boldsymbol{u}} + \frac{\dot{p}}{Q} = 0, \qquad \text{with} \quad \frac{1}{Q} = \frac{n}{K_f} + \frac{\alpha - n}{K_s}, \tag{5}$$

with $(1/Q)$ commonly referred to as the hydraulic capacity and K_f the bulk modulus of the fluid phase. Eq. (5) takes into account that both fluid flow (through $\boldsymbol{w}$) and undrained compression (through $\dot{p}$) will cause volume changes of the porous medium,

The three governing equations, Eqs. (3), (4) and (5), together with the stress decomposition, Eq. (1), and the constitutive relation, Eq. (2), describe the hydro-mechanical behavior of the saturated porous medium under general static and dynamic conditions. The model based on Eqs. (3) to (5) is known as the $\boldsymbol{u}$-$\boldsymbol{w}$-p formulation, in correspondence with unknown primary variables that need to be solved, i.e., the displacement $\boldsymbol{u}$ of the solid phase, the Darcy velocity $\boldsymbol{w}$ of the fluid phase, and the pressure p of the fluid phase.

The convective fluid acceleration term $(\dot{\boldsymbol{w}} + (\boldsymbol{\nabla w})\,\boldsymbol{w})$ appearing in Eqs. (3) and (4) is generally relatively small, and therefore can be omitted (Zienkiewicz et al., 1999). Accordingly, Eq. (3) reduces to

$$\boldsymbol{\nabla}\cdot\boldsymbol{\sigma} - \rho\ddot{\boldsymbol{u}} + \rho\boldsymbol{b} = \boldsymbol{0}, \tag{6}$$

while the reduced form of Eq. (4) can be rewritten into an expression for the viscous drag force $\boldsymbol{R}$, which, followed by invoking Darcy's seepage law and substituting the result into Eq. (5), leads to

$$\boldsymbol{\nabla}\cdot\left[k\left(-\boldsymbol{\nabla}p - \rho_f\ddot{\boldsymbol{u}} + \rho_f\boldsymbol{b}\right)\right] + \alpha\boldsymbol{\nabla}\cdot\dot{\boldsymbol{u}} + \frac{\dot{p}}{Q} = 0. \tag{7}$$

Note that the reduced set of the two governing equations above is independent of the Darcy velocity $\boldsymbol{w}$, and therefore is known as the $\boldsymbol{u}$–p formulation (Zienkiewicz et al., 1999). It should be noted that the $\boldsymbol{u}$–p formulation may lose accuracy in specific problems involving high-frequency, short-duration dynamic phenomena, such as those induced by very rapid loading. In such cases, strong hydro-mechanical coupling and oscillatory responses may develop in the displacement and pore-pressure fields, and the simplifying assumptions adopted in the present formulation may no longer be appropriate. For these situations, the more general $\boldsymbol{u}$–$\boldsymbol{w}$–p formulation, which retains the convective fluid acceleration terms, generally provides a more accurate description of the coupled dynamics (Zienkiewicz et al., 1999).

To complete the strong form of the initial–boundary value problem, the $\boldsymbol{u}$–p formulation is supplemented with appropriate initial and boundary conditions. Fig. 1a schematically shows a domain Ω containing a saturated porous medium. The domain is bounded by the outer

domain boundary Γ of which the outward unit normal vector is $\boldsymbol{n}_\Gamma$. Accordingly, the closure of Ω equals $\overline{\Omega} = \Omega \cup \Gamma$. The outer domain boundary is composed of subboundaries at which essential (Dirichlet) and natural (Neumann) boundary conditions are prescribed, which, respectively, are denoted as Γ_u and Γ_t for the mechanical problem, and as Γ_p and Γ_q for the hydrological problem. In correspondence with the definition of Γ, the composition of the boundary can expressed as $\Gamma = \overline{\Gamma_u \cup \Gamma_t} = \overline{\Gamma_p \cup \Gamma_q}$, with the condition that the subboundaries are disjoint as $\Gamma_u \cap \Gamma_t = \Gamma_p \cap \Gamma_q = \varnothing$. The domain is composed of two material phases Ω_i, with $i = \{1,2\}$, so that $\overline{\Omega} = \cup_i \overline{\Omega}_i$. Hence, the material interface between the two subdomains is defined by $\Gamma_{12} = \overline{\Omega}_1 \cap \overline{\Omega}_2$, with its unit normal vector given by $\boldsymbol{n}_{12}$. Further, the initial conditions at $t = 0$ read

$$\boldsymbol{u}(\boldsymbol{x},0) = \boldsymbol{u}^0(\boldsymbol{x},0) \qquad \text{in } \Omega, \tag{8}$$

$$\dot{\boldsymbol{u}}(\boldsymbol{x},0) = \dot{\boldsymbol{u}}^0(\boldsymbol{x},0) \qquad \text{in } \Omega, \tag{9}$$

$$p(\boldsymbol{x},0) = p^0(\boldsymbol{x},0) \qquad \text{in } \Omega, \tag{10}$$

where $\boldsymbol{u}^0$, and $\dot{\boldsymbol{u}}^0$ denote the initial values of the displacement and velocity fields of the solid phase, respectively, and p^0 represents the initial values of the fluid pressure field. The time-dependent behavior of the porous medium will be analyzed up to a predefined, maximum time T, so that $t \in [0,T]$. The mechanical boundary conditions within this time domain are defined by

$$\boldsymbol{u}(\boldsymbol{x},t) = \bar{\boldsymbol{u}}(\boldsymbol{x},t) \qquad \text{on } \Gamma_u \times [0,T], \tag{11}$$

$$\boldsymbol{t}(\boldsymbol{x},t) = \boldsymbol{n}_\Gamma(\boldsymbol{x}) \cdot \boldsymbol{\sigma}(\boldsymbol{x},t) = \bar{\boldsymbol{t}}(\boldsymbol{x},t) \qquad \text{on } \Gamma_t \times [0,T], \tag{12}$$

where $\boldsymbol{t}$ denotes the traction, and $\bar{\boldsymbol{u}}$ and $\bar{\boldsymbol{t}}$ are the displacements and tractions prescribed at the boundary, respectively. Additionally, the mechanical continuity conditions at the material interface are

$$[\![\boldsymbol{u}]\!] = \boldsymbol{0} \qquad \text{on } \Gamma_{12} \times [0,T], \tag{13}$$

$$[\![\boldsymbol{t}]\!] = [\![\boldsymbol{n}_{12} \cdot \boldsymbol{\sigma}]\!] = \boldsymbol{0} \qquad \text{on } \Gamma_{12} \times [0,T], \tag{14}$$

where $[\![\cdot]\!]$ denotes the jump in the corresponding field variable, as computed after evaluating its value at either side, $\boldsymbol{x}^+$ and $\boldsymbol{x}^-$, of the material interface. Note that, for ease of interpretation, in Eqs. (13) and (14) the dependency of the variables on space and time, which is comparable as presented for the boundary conditions Eqs. (11) and (12), has been omitted. Similar to the mechanical boundary conditions, the hydrological boundary conditions read

$$p(\boldsymbol{x},t) = \bar{p}(\boldsymbol{x},t) \qquad \text{on } \Gamma_p \times [0,T], \tag{15}$$

$$q(\boldsymbol{x},t) = \boldsymbol{n}_\Gamma(\boldsymbol{x}) \cdot \boldsymbol{w}(\boldsymbol{x},t) = \bar{q}(\boldsymbol{x},t) \qquad \text{on } \Gamma_q \times [0,T], \tag{16}$$

in which q is the fluid flux normal to the outer boundary. Further, the hydrological continuity conditions at the material interface are

$$[\![p]\!] = 0 \qquad \text{on } \Gamma_{12} \times [0,T], \tag{17}$$

$$[\![q]\!] = [\![\boldsymbol{n}_{12} \cdot \boldsymbol{w}]\!] = 0 \quad \text{on } \Gamma_{12} \times [0,T], \tag{18}$$

where, in Eqs. (16) and (18), the Darcy velocity $\boldsymbol{w}$ in the $\boldsymbol{u} - p$ formulation follows from

$$\boldsymbol{w} = -k\left(\boldsymbol{\nabla} p + \rho_f \ddot{\boldsymbol{u}} - \rho_f \boldsymbol{b}\right). \tag{19}$$

Using the above formulation, we will seek for solutions for the displacement field $\boldsymbol{u}(\boldsymbol{x},t)$ and the pressure field $p(\boldsymbol{x},t)$ that are continuous within the domain Ω, while their spatial gradients show a jump across the material interface Γ_{12}, i.e., $[\![\boldsymbol{n}_{12} \cdot \boldsymbol{\nabla u}]\!] \neq 0$ and $[\![\boldsymbol{n}_{12} \cdot \boldsymbol{\nabla} p]\!] \neq 0$. The accurate modeling of these weak discontinuities ensures that the numerical results obtained by IGFEM with a *nonconformal mesh* at the material interface, see Fig. 1b, can be adequately compared to the results obtained by standard FEM with a *conformal mesh* at the material interface. It is important to mention that Eq. (13) assumes that the material interface is *coherent*, i.e., at the material interface the two solid phases are perfectly bonded and undamaged. The presence of damage (fracture, cavities) or plastic slip at the interface results in a strong discontinuity in the local displacement field that will alter the hydro-mechanical response of the surrounding porous medium; the consideration of this aspect, however, falls beyond the scope of the present work.

2.2. Weak formulation of the problem

The weak form of the two governing Eqs. (6) and (7) is obtained by multiplying these equations by admissible test functions $\delta\boldsymbol{u}$ and δp, respectively, and integrating the expressions over the domain Ω. The trial displacement and pressure fields, together with their corresponding test functions, are assumed to belong to appropriate functional spaces. Specifically, the trial and test functions are defined over the domain such that square integrability is satisfied over the entire domain Ω, while first-order Sobolev regularity is required within each material subdomain, i.e., we use "broken" Sobolev spaces. Mathematically, we define the scalar-valued set $\mathcal{V}(\Omega) = \left\{v \in \mathcal{L}^2(\Omega),\, v|_{\Omega_i} \in \mathcal{H}^1(\Omega_i)\right\}$. The displacement field is then taken from the vector-valued space $\boldsymbol{\mathcal{V}}_u(\Omega) = \left\{\boldsymbol{u} |\, \boldsymbol{u} \in [\mathcal{V}(\Omega)]^2, \boldsymbol{u}|_{\Gamma_u} = \boldsymbol{0}\right\}$ and the pressure field from $\mathcal{V}_p(\Omega) = \left\{p |\, p \in \mathcal{V}(\Omega), p|_{\Gamma_p} = 0\right\}$. Noteworthy, while we use these spaces when dealing with homogeneous Dirichlet boundary conditions on both displacement and pressure fields, we can still use these spaces when dealing with non-homogeneous conditions by simply defining a so-called *linear variety* (Aragón and Duarte, 2023, Sec. 2.1.2.2). After applying the divergence theorem and using the definitions in Eqs. (12) and (16), this leads to

$$\int_\Omega \boldsymbol{\sigma} : \delta\boldsymbol{\epsilon}\, \mathrm{d}\Omega + \int_\Omega \rho\, \ddot{\boldsymbol{u}} \cdot \delta\boldsymbol{u}\, \mathrm{d}\Omega - \int_\Omega \rho\, \boldsymbol{b} \cdot \delta\boldsymbol{u}\, \mathrm{d}\Omega - \int_{\Gamma_t} \bar{\boldsymbol{t}} \cdot \delta\boldsymbol{u}\, \mathrm{d}\Gamma_t + \int_{\Gamma_{12}} [\![\boldsymbol{t} \cdot \delta\boldsymbol{u}]\!]\, \mathrm{d}\Gamma_{12} = 0 \qquad \forall \delta\boldsymbol{u} \in \boldsymbol{\mathcal{V}}_u, \tag{20}$$

and

$$\int_\Omega k \boldsymbol{\nabla} p \cdot \boldsymbol{\nabla} \delta p\, \mathrm{d}\Omega + \int_\Omega k \rho_f \ddot{\boldsymbol{u}} \cdot \boldsymbol{\nabla} \delta p\, \mathrm{d}\Omega + \int_\Omega \alpha \boldsymbol{\nabla} \cdot \dot{\boldsymbol{u}}\, \delta p\, \mathrm{d}\Omega + \int_\Omega \frac{\dot{p}}{Q} \delta p\, \mathrm{d}\Omega - \int_\Omega k \rho_f \boldsymbol{b} \cdot \boldsymbol{\nabla} \delta p\, \mathrm{d}\Omega + \int_{\Gamma_q} \bar{q}\, \delta p\, \mathrm{d}\Gamma_q - \int_{\Gamma_{12}} [\![q\, \delta p]\!]\, \mathrm{d}\Gamma_{12} = 0 \quad \forall \delta p \in \mathcal{V}_p, \tag{21}$$

where $\delta\boldsymbol{\epsilon} = \frac{1}{2}\left(\boldsymbol{\nabla}\delta\boldsymbol{u} + (\boldsymbol{\nabla}\delta\boldsymbol{u})^\top\right)$ and the symmetry of the Cauchy stress tensor, $\boldsymbol{\sigma} = \boldsymbol{\sigma}^\top$, has been utilized. Note that the terms in Eqs. (20) and (21) related to a jump across the material interface vanish, because of the interface continuity conditions provided by Eqs. (13), (14), (17) and (18). Hence, Eqs. (20) and (21) reduce to

$$\int_\Omega \boldsymbol{\sigma} : \delta\boldsymbol{\epsilon}\, \mathrm{d}\Omega + \int_\Omega \rho \ddot{\boldsymbol{u}} \cdot \delta\boldsymbol{u}\, \mathrm{d}\Omega = \int_\Omega \rho\, \boldsymbol{b} \cdot \delta\boldsymbol{u}\, \mathrm{d}\Omega + \int_{\Gamma_t} \bar{\boldsymbol{t}} \cdot \delta\boldsymbol{u}\, \mathrm{d}\Gamma_t \qquad \forall \delta\boldsymbol{u} \in \boldsymbol{\mathcal{V}}_u, \tag{22}$$

and

$$\int_\Omega k \boldsymbol{\nabla} p \cdot \boldsymbol{\nabla} \delta p\, \mathrm{d}\Omega + \int_\Omega k \rho_f \ddot{\boldsymbol{u}} \cdot \boldsymbol{\nabla} \delta p\, \mathrm{d}\Omega + \int_\Omega \alpha \boldsymbol{\nabla} \cdot \dot{\boldsymbol{u}}\, \delta p\, \mathrm{d}\Omega + \int_\Omega \frac{\dot{p}}{Q} \delta p\, \mathrm{d}\Omega = \int_\Omega k \rho_f \boldsymbol{b} \cdot \boldsymbol{\nabla} \delta p\, \mathrm{d}\Omega - \int_{\Gamma_q} \bar{q}\, \delta p\, \mathrm{d}\Gamma_q \qquad \forall \delta p \in \mathcal{V}_p. \tag{23}$$

In the above expressions, the terms at the left-hand sides depend on both the primary field variables $\boldsymbol{u}$ and p and the test functions $\delta\boldsymbol{u}$ and δp, while the terms on the right-hand sides depend on the test functions only. Correspondingly, the coupled set of Eqs. (22) and (23) can be formally expressed as: Find $\boldsymbol{u}, p \in \boldsymbol{\mathcal{V}}_u \times \mathcal{V}_p$ such that

$$\mathcal{B}_u(\boldsymbol{u}, p, \delta\boldsymbol{u}) = \mathcal{L}_u(\delta\boldsymbol{u}) \quad \forall \delta\boldsymbol{u} \in \boldsymbol{\mathcal{V}}_u \quad \text{and} \quad \mathcal{B}_p(\boldsymbol{u}, p, \delta p) = \mathcal{L}_p(\delta p) \quad \forall \delta p \in \mathcal{V}_p, \tag{24}$$

where the bilinear forms $\mathcal{B}_u$ and $\mathcal{B}_p$ and linear forms $\mathcal{L}_u$ and $\mathcal{L}_p$ may be respectively inferred from the left-hand sides and right-hand sides of Eqs. (22) and (23).

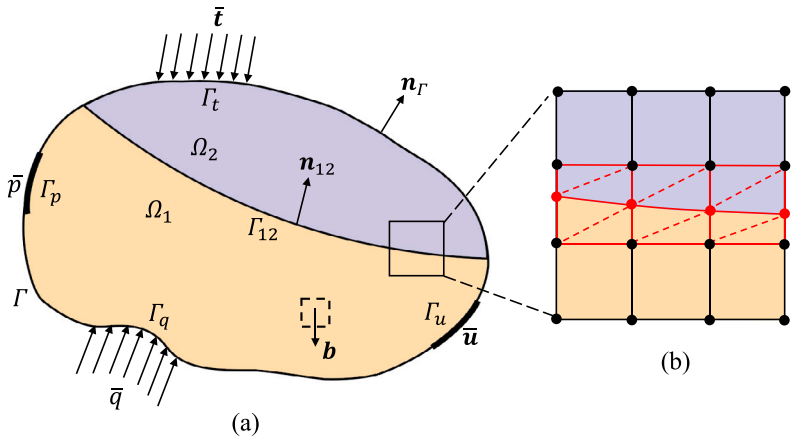

Fig. 1. (a) Schematic 2D representation of a porous medium with a domain Ω, and an external boundary Γ with outer unit normal vector $\boldsymbol{n}_\Gamma$. The porous medium contains a material interface Γ_{12} with unit normal vector $\boldsymbol{n}_{12}$ that separates two distinct material phases Ω_i, with $i = \{1, 2\}$. The domain is subjected to prescribed displacements $\bar{\boldsymbol{u}}$ on Γ_u, prescribed tractions $\bar{\boldsymbol{t}}$ on Γ_t, a prescribed fluid pressure $\bar{p}$ on Γ_p, a prescribed fluid flux $\bar{q}$ on Γ_q, and a body force per unit volume $\boldsymbol{b}$. (b) Nonconformal mesh at the material interface Γ_{12}, with the standard nodes and enriched nodes of the nonconformal continuum elements indicated by black and red solid circles, respectively. The enriched nodes are placed at the intersections between the material interface and the element edges of nonconformal continuum elements, thereby leading to the introduction of so-called *cut elements* that are subsequently subdivided (as indicated by the red dashed lines) into four triangular *integration elements*.

2.3. Interface-enriched generalized finite element discretization

In order to solve the finite-dimensional counterparts of Eqs. (22) and (23), the domain Ω is discretized with a mesh of quadrilateral finite elements that do not conform to the material interface, and the interface-generalized finite element method (IGFEM) is adopted to recover the otherwise lost accuracy. This is schematically shown in Fig. 1b. Enriched nodes are introduced at the intersections of the material interface Γ_{12} with the edges of nonconformal continuum elements, resulting in the formation of so-called *cut elements*. The cut elements are subsequently subdivided into triangular *integration elements*, used for performing the integration of local arrays over the cut elements.

Following a Bubnov–Galerkin procedure, the trial and test functions associated with the displacement field in the solid matrix are chosen from the same IGFEM enriched space $\mathcal{V}_u^h(\Omega^h) \subset \mathcal{V}_u(\Omega)$. The discrete displacement field is approximated as

$$\boldsymbol{u}^h(\boldsymbol{x}, t) = \underbrace{\sum_{i \in \iota_h} N_i(\boldsymbol{x})\, \tilde{\boldsymbol{u}}_i(t)}_{\text{standard FEM}} + \underbrace{\sum_{i \in \iota_w} \psi_i(\boldsymbol{x})\, \boldsymbol{\alpha}_i(t)}_{\text{enrichment}}, \quad \tilde{\boldsymbol{u}}_i, \boldsymbol{\alpha}_i \in \mathbb{R}^2, \tag{25}$$

and the test functions are defined analogously. Likewise, the trial and test functions for the fluid pressure field are taken from the finite-dimensional space $\mathcal{V}_p^h(\Omega^h) \subset \mathcal{V}_p(\Omega)$, and the discrete pressure field is given by

$$p^h(\boldsymbol{x}, t) = \underbrace{\sum_{i \in \iota_h} N_i(\boldsymbol{x})\, \tilde{p}_i(t)}_{\text{standard FEM}} + \underbrace{\sum_{i \in \iota_w} \psi_i(\boldsymbol{x})\, \gamma_i(t)}_{\text{enrichment}}, \quad \tilde{p}_i, \gamma_i \in \mathbb{R}, \tag{26}$$

with test functions defined in the same manner. In Eqs. (25) and (26), the first terms correspond to the standard FEM approximation, with ι_h denoting the index set of standard nodes of the original mesh (indicated by the black solid circles in Fig. 1b), and the second terms correspond to the enrichment, with ι_w denoting the index set of enriched nodes of cut elements (indicated by the red solid circles in Fig. 1b). In the first terms, N_i is the standard Lagrangian shape function associated with the ith mesh node, and $\tilde{\boldsymbol{u}}_i$ and $\tilde{p}_i$, represent the corresponding standard DOFs of solid matrix displacement and fluid pressure, respectively. In the second terms, ψ_i is the enrichment function, and $\boldsymbol{\alpha}_i$ and γ_i represent the enriched DOFs of solid displacement and fluid pressure associated with the ith enriched node, respectively. C^0-continuity is ensured by sharing enriched nodes between neighboring cut elements, since these nodes

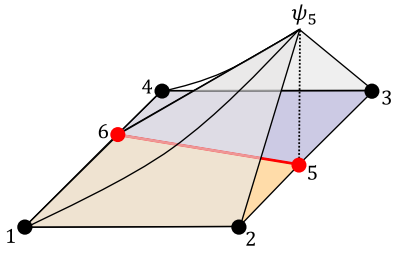

Fig. 2. Schematic of weakly-discontinuous enrichment function ψ_5, which is constructed with the aid of Lagrangian shape functions in child quadrilateral elements. The enrichment function obtains its maximum value of one at the corresponding enriched node $\boldsymbol{x}_5$ and decreases to zero at the location of standard nodes $\{\boldsymbol{x}_i\}_{i=1}^4$. Standard and enriched nodes are designated by, respectively, black and red solid circles.

are placed at interface-edge intersections on edges that are typically common to adjacent elements.

The enrichment term enhances the standard finite element approximation through weakly-discontinuous enrichment functions ψ_i, which incorporate the discontinuities in the solid matrix displacement gradient and fluid pressure gradient along the material interface Γ_{12}. Consider the case where the material interface divides a quadrilateral cut element into two quadrilateral subdomains (see Fig. 2), which we refer to as *child elements*. In this case, the enrichment function ψ_i is constructed with the aid of Lagrangian shape functions in these two quadrilateral subdomains (Soghrati et al., 2012). The enrichment function obtains its maximum value of one at the corresponding enriched nodes, and decreases to zero at the location of standard nodes of the cut element. Therefore, the enrichment functions are identically zero in *blending elements* (i.e., the elements adjacent to cut elements); as a result, there is no reduced accuracy nor degraded rate of convergence due to parasitic terms in blending elements. Child elements are further partitioned into *integration elements*, which are generated specifically for Gauss quadrature of local element arrays, as explained in more detail below. It is worth noting that the material interface may also divide a quadrilateral parent element into two triangular subdomains (the interface passing through two opposing nodes), or create one triangular and one pentagonal subdomain (the interface cuts two neighboring edges of a quadrangle). IGFEM is capable of handling such cases as well, as

explained in Aragón et al. (2020); a detailed treatment of quadrilateral parent elements divided into a triangular and a pentagonal subdomain is provided in the context of the hydro-mechanical problem presented in Section 3.4. Furthermore, IGFEM has been extended to accommodate multiple interfaces intersecting a single element through the Hierarchical Interface-enriched Finite Element Method (HIFEM) (Soghrati, 2014; Aragón et al., 2020). In HIFEM, enrichment functions are constructed hierarchically, where child elements generated by an initial interface act as parents to subsequent child elements formed by additional interfaces, resulting in a hierarchy organized within an ordered tree structure.

Inserting the approximation functions for the solid matrix displacement (25) and fluid pressure (26) together with the stress decomposition (1) and constitutive relation (2) into the weak forms (22) and (23), and requiring that these equations must hold for arbitrary test functions $\delta\boldsymbol{u}$ and δp, we obtain the spatially discretized variational forms of the governing equations. For the standard, uncut elements that are not intersected by material interfaces, the local arrays are constructed by means of the usual finite element operations. Additionally, for a cut element e with element boundary ∂e, the spatially discretized forms of the governing equations are represented by the element-level contributions

$$\underbrace{\left(\int_e \boldsymbol{N}_U^\top\, \rho\, \boldsymbol{N}_U \,\mathrm{d}e\right)}_{\boldsymbol{m}_e} \ddot{\boldsymbol{U}}_e + \underbrace{\left(\int_e \boldsymbol{B}_U^\top\, \boldsymbol{D}\, \boldsymbol{B}_U \,\mathrm{d}e\right)}_{\boldsymbol{k}_e} \boldsymbol{U}_e - \underbrace{\left(\int_e \boldsymbol{B}_U^\top\, \alpha \boldsymbol{r}\, \boldsymbol{N}_P \,\mathrm{d}e\right)}_{\boldsymbol{g}_e} \boldsymbol{P}_e = \underbrace{\left(\int_e \boldsymbol{N}_U^\top \rho \boldsymbol{b}\,\mathrm{d}e + \int_{\partial e\cap\Gamma_t} \boldsymbol{N}_U^\top\, \bar{\boldsymbol{t}}\,\mathrm{d}\partial e\right)}_{\boldsymbol{f}_e^U}, \tag{27}$$

and

$$\begin{aligned}&\underbrace{\left(\int_e (\boldsymbol{\nabla N}_P)^\top\, k\rho_f \boldsymbol{N}_U \,\mathrm{d}e\right)}_{\boldsymbol{c}_e} \dot{\boldsymbol{U}}_e + \underbrace{\left(\int_e \boldsymbol{N}_P^\top\, \alpha \boldsymbol{r}^\top \boldsymbol{B}_U \,\mathrm{d}e\right)}_{\boldsymbol{g}_e^\top} \dot{\boldsymbol{U}}_e \\ &+ \underbrace{\left(\int_e (\boldsymbol{\nabla N}_P)^\top\, k\, (\boldsymbol{\nabla N}_P) \,\mathrm{d}e\right)}_{\boldsymbol{h}_e} \boldsymbol{P}_e + \underbrace{\left(\int_e \boldsymbol{N}_P^\top\, \frac{1}{Q}\, \boldsymbol{N}_P \,\mathrm{d}e\right)}_{\boldsymbol{s}_e} \dot{\boldsymbol{P}}_e \\ &= \underbrace{\left(\int_e (\boldsymbol{\nabla N}_P)^\top\, k\rho_f \boldsymbol{b}\,\mathrm{d}e - \int_{\partial e\cap\Gamma_q} \boldsymbol{N}_P^\top\, \bar{q}\,\mathrm{d}\partial e\right)}_{\boldsymbol{f}_e^P}.\end{aligned} \tag{28}$$

In the above equations, the local arrays $\boldsymbol{m}_e$, $\boldsymbol{k}_e$, $\boldsymbol{g}_e$, $\boldsymbol{c}_e$, $\boldsymbol{h}_e$, and $\boldsymbol{s}_e$ represent the elements' mass matrix, stiffness matrix, coupling matrix, inertia matrix, permeability matrix, and compressibility matrix, respectively. Additionally, $\boldsymbol{f}_e^U$ and $\boldsymbol{f}_e^P$ reflect the elements' external force vector and flux vector, respectively. Furthermore, $\boldsymbol{U}_e = \begin{bmatrix}\boldsymbol{u}_e & \boldsymbol{\alpha}_e\end{bmatrix}^\top$, where $\boldsymbol{u}_e$ and $\boldsymbol{\alpha}_e$ respectively are the standard and enriched degrees of freedom that define the solid matrix displacement field; similarly, $\boldsymbol{P}_e = \begin{bmatrix}\boldsymbol{p}_e & \boldsymbol{\gamma}_e\end{bmatrix}^\top$, where $\boldsymbol{p}_e$ and $\boldsymbol{\gamma}_e$ respectively are the vectors of standard and enriched DOFs that define the fluid pressure field. Moreover, $\boldsymbol{N}_U = \begin{bmatrix}\boldsymbol{N}_u & \boldsymbol{\psi}_\alpha\end{bmatrix}^\top$, with $\boldsymbol{N}_u$ and $\boldsymbol{\psi}_\alpha$ denoting the elements' standard shape function matrix and enrichment function matrix of the solid matrix displacement field, respectively; similarly, $\boldsymbol{N}_P = \begin{bmatrix}\boldsymbol{N}_p & \boldsymbol{\psi}_\gamma\end{bmatrix}^\top$, with $\boldsymbol{N}_p$ and $\boldsymbol{\psi}_\gamma$ denoting the elements' standard shape function matrix and enrichment function matrix of the fluid pressure field, respectively. Additionally, $\boldsymbol{B}_U = [\partial \boldsymbol{N}_u \quad \partial \boldsymbol{\psi}_\alpha]$ is the elements' strain–displacement matrix, with the differential operator ∂ for a two-dimensional problem defined by

$$\boldsymbol{\partial} \equiv \begin{bmatrix}\partial/\partial x & 0 & \partial/\partial y \\ 0 & \partial/\partial y & \partial/\partial x\end{bmatrix}^\top. \tag{29}$$

Finally, the term r appearing in Eq. (28) for a two-dimensional formulation reads $\boldsymbol{r} = [1\ 1\ 0]^\top$.

To perform the numerical integration of local arrays over cut elements, these elements are subdivided into integration elements that conform to the discontinuity, i.e., the discontinuity aligns with edges of integration elements (Khoei, 2014; Aragón et al., 2020), see Fig. 1b. This approach avoids integrating a non-smooth function, allowing the use of the minimum number of Gaussian quadrature points. Consider the eth triangular integration element, which is generated within the quadrilateral cut element, see Fig. 3a. The numerical quadrature for this element is carried out on its corresponding master triangular element $\triangle$ defined by the reference coordinates $\boldsymbol{\xi} = (\xi, \eta)$, see Fig. 3b. Accordingly, for the triangular integration element, as an example, the mass matrix is numerically computed as

$$\begin{aligned}\boldsymbol{m}_e &= \int_e \boldsymbol{N}_U^\top\, \rho\, \boldsymbol{N}_U \,\mathrm{d}e_1 = \int_\triangle \boldsymbol{N}_U^\top\, \rho\, \boldsymbol{N}_U\, j\,\mathrm{d}\triangle \\ &= \sum_{i=1}^{n_{\mathrm{GP}}} \boldsymbol{N}_U^\top\,(\boldsymbol{\xi}_i)\,\rho\,(\boldsymbol{\xi}_i)\,\boldsymbol{N}_U\,(\boldsymbol{\xi}_i)\,w_i\,j,\end{aligned} \tag{30}$$

in which, $\boldsymbol{\xi}_i = (\xi_i, \eta_i)$ denotes the reference coordinates of the Gaussian quadrature point i in the master integration element, w_i is the corresponding weight, and j represents the Jacobian of the geometric mapping. It is noteworthy that $\boldsymbol{N}_U$ contains shape functions of the quadrilateral cut element, for which we need to find the reference coordinates $\boldsymbol{\xi}$ of the integration points on the master quadrilateral element $\square$ shown in Fig. 3b. To this end, for a given Gaussian quadrature point i on the master triangular element $\triangle$, the reference coordinate $\boldsymbol{\xi}_i$ is first mapped to the physical coordinate $\boldsymbol{x}_i$, after which the reference coordinate $\boldsymbol{\xi}_i$ defined by the subsequent mapping on the master quadrilateral element $\square$ is calculated via a Newton–Raphson procedure (i.e., due to the nonlinear nature of this isoparametric mapping, a corresponding nonlinear equation needs to be solved). For more details, we refer to Aragón and Duarte (2023). The remaining local arrays in Eqs. (27) and (28) are similarly evaluated via numerical integration over the integration elements.

The global arrays are constructed by assembling the contributions of all elements, i.e.,

$$\begin{aligned}&\boldsymbol{M} = \mathop{\mathbb{A}}_{e=1}^{N_e} \boldsymbol{m}_e, \quad \boldsymbol{K} = \mathop{\mathbb{A}}_{e=1}^{N_e} \boldsymbol{k}_e, \quad \boldsymbol{G} = \mathop{\mathbb{A}}_{e=1}^{N_e} \boldsymbol{g}_e, \quad \boldsymbol{C} = \mathop{\mathbb{A}}_{e=1}^{N_e} \boldsymbol{c}_e, \\ &\boldsymbol{H} = \mathop{\mathbb{A}}_{e=1}^{N_e} \boldsymbol{h}_e, \quad \boldsymbol{S} = \mathop{\mathbb{A}}_{e=1}^{N_e} \boldsymbol{s}_e, \quad \boldsymbol{F}^U = \mathop{\mathbb{A}}_{e=1}^{N_e} \boldsymbol{f}_e^U, \quad \boldsymbol{F}^P = \mathop{\mathbb{A}}_{e=1}^{N_e} \boldsymbol{f}_e^P,\end{aligned} \tag{31}$$

in which $\mathbb{A}$ denotes the standard finite element assembly operator and N_e is the number of elements in the IGFEM mesh, i.e., the standard (uncut) elements and integration elements of cut elements. Combining Eqs. (27) and (28) with Eq. (31), the system of coupled, discretized

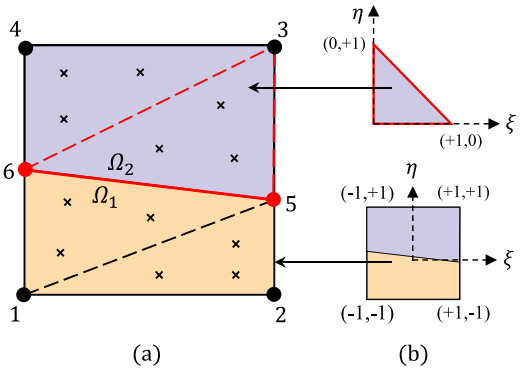

Fig. 3. (a) Subdivision of a quadrilateral cut element into four triangular integration elements in order to perform the numerical quadrature. The black and red solid circles show the standard and enriched nodes, respectively, and the black crosses represent the Gaussian quadrature points inside integration elements. (b) Triangular and quadrilateral master elements used for the two isoparametric mappings involved in the computation of local arrays.

governing equations of the hydro-mechanical model becomes

$$\begin{aligned} \boldsymbol{M}\ddot{\boldsymbol{U}} + \boldsymbol{K}\boldsymbol{U} - \boldsymbol{G}\boldsymbol{P} &= \boldsymbol{F}^{U}, \\ \boldsymbol{C}\ddot{\boldsymbol{U}} + \boldsymbol{G}^{\top}\dot{\boldsymbol{U}} + \boldsymbol{H}\boldsymbol{P} + \boldsymbol{S}\dot{\boldsymbol{P}} &= \boldsymbol{F}^{P}, \end{aligned} \tag{32}$$

where $\boldsymbol{U} = [\boldsymbol{u}\ \ \boldsymbol{\alpha}]^{\top}$ and $\boldsymbol{P} = [p\ \ \gamma]^{\top}$ respectively are the arrays containing the solid matrix displacements and fluid pressures at standard and enriched DOFs, evaluated in the global reference system.

2.4. Monolithic update scheme

To obtain the numerical solution, the coupled Eqs. (32) must be also discretized in the time domain, for which we employ the generalized Newmark method (Newmark, 1959). At each incremental time step $[t_n, t_{n+1}]$, the unknown values of primary variables—solid matrix displacement and fluid pressure—and their time derivatives need to be calculated at time $t_{n+1} = t_n + \Delta t$, assuming the values at the previous time step t_n are known. Following Zienkiewicz et al. (1999), the relations between the unknown values of the displacements and their time derivatives at the current time t_{n+1} and the known values at the previous time t_n are computed in accordance with the second-order time integration scheme

$$\begin{aligned} \ddot{\boldsymbol{U}}_{n+1} &= \ddot{\boldsymbol{U}}_n + \Delta\ddot{\boldsymbol{U}}_n, \\ \dot{\boldsymbol{U}}_{n+1} &= \dot{\boldsymbol{U}}_n + \ddot{\boldsymbol{U}}_n\Delta t + \beta_1\Delta\ddot{\boldsymbol{U}}_n\Delta t, \\ \boldsymbol{U}_{n+1} &= \boldsymbol{U}_n + \dot{\boldsymbol{U}}_n\Delta t + \frac{1}{2}\ddot{\boldsymbol{U}}_n\Delta t^2 + \frac{1}{2}\beta_2\Delta\ddot{\boldsymbol{U}}_n\Delta t^2, \end{aligned} \tag{33}$$

where the subscripts n and $n+1$ designate the time steps at which the variables are computed. Additionally, the relationships between the unknown pressure values and their time derivatives at time t_{n+1}, and the known values at time t_n, are determined using a first-order time integration scheme

$$\begin{aligned} \dot{\boldsymbol{P}}_{n+1} &= \dot{\boldsymbol{P}}_n + \Delta\dot{\boldsymbol{P}}_n, \\ \boldsymbol{P}_{n+1} &= \boldsymbol{P}_n + \dot{\boldsymbol{P}}_n\Delta t + \bar{\beta}_1\Delta\dot{\boldsymbol{P}}_n\Delta t. \end{aligned} \tag{34}$$

The use of a second-order time integration scheme for the displacement field, Eq. (33), and a first-order scheme for the pressure field, Eq. (34), reflects the respective differential orders of the governing equations in Eq. (32). This mixed-order time discretization ensures a consistent and accurate treatment of the coupled $\boldsymbol{u}$–p formulation (Zienkiewicz et al., 1999). The Newmark method, which is an implicit time integration scheme, can be made unconditionally stable when the Newmark parameters β_1, β_2 and $\bar{\beta}_1$ in Eqs. (33) and (34) meet the requirements (Bathe, 1982; Hughes, 1987):

$$\beta_1 \geq \frac{1}{2}, \qquad \beta_2 \geq \frac{1}{2}\left(\beta_1 + \frac{1}{2}\right)^2 \quad \text{and} \quad \bar{\beta}_1 \geq \frac{1}{2}. \tag{35}$$

A special case of the Newmark scheme is the trapezoidal rule, obtained by setting $\beta_1 = \beta_2 = \bar{\beta}_1 = 0.5$. While this choice satisfies the unconditional stability requirements of Eq. (35), it introduces no numerical (algorithmic) damping and can therefore lead to spurious numerical oscillations when the system exhibits insufficient physical damping (Zienkiewicz et al., 1999). To mitigate this issue, slightly larger parameter values are often adopted in practice to introduce algorithmic damping and suppress high-frequency oscillations in transient responses. For example, the Newmark parameters $\beta_1 = \bar{\beta}_1 = 0.6$ and $\beta_2 = 0.605$ are recommended in Zienkiewicz et al. (1999) and are therefore adopted in the boundary value problems considered in this study. Inserting Eqs. (33) and (34) into Eqs. (32) leads to the coupled, nonlinear algebraic equations

$$\begin{aligned} \boldsymbol{\Psi}^{U}_{n+1} = &\left(\frac{1}{\beta_1\Delta t^2}\boldsymbol{M} + \boldsymbol{K}\right)\boldsymbol{U}_{n+1} - \boldsymbol{G}\,\boldsymbol{P}_{n+1} \\ &- \boldsymbol{M}\left(\frac{1}{\beta_1\Delta t^2}\boldsymbol{U}_n + \frac{1}{\beta_1\Delta t}\dot{\boldsymbol{U}}_n + \left(\frac{1}{2\beta_1} - 1\right)\ddot{\boldsymbol{U}}_n\right) - \boldsymbol{F}^{U} = \boldsymbol{0}, \end{aligned} \tag{36}$$

and

$$\begin{aligned} \boldsymbol{\Psi}^{P}_{n+1} = &\left(\frac{1}{\beta_1\Delta t^2}\boldsymbol{C} + \frac{\beta_2}{\beta_1\Delta t}\boldsymbol{G}^{\top}\right)\boldsymbol{U}_{n+1} + \left(\boldsymbol{H} + \frac{1}{\bar{\beta}_1\Delta t}\boldsymbol{S}\right)\boldsymbol{P}_{n+1} \\ &- \boldsymbol{C}\left(\frac{1}{\beta_1\Delta t^2}\boldsymbol{U}_n + \frac{1}{\beta_1\Delta t}\dot{\boldsymbol{U}}_n + \left(\frac{1}{2\beta_1} - 1\right)\ddot{\boldsymbol{U}}_n\right) \\ &- \boldsymbol{G}^{\top}\left(\frac{\beta_2}{\beta_1\Delta t}\boldsymbol{U}_n + \left(\frac{\beta_2}{\beta_1} - 1\right)\dot{\boldsymbol{U}}_n + \Delta t\left(\frac{\beta_2}{2\beta_1} - 1\right)\ddot{\boldsymbol{U}}_n\right) \\ &- \boldsymbol{S}\left(\frac{1}{\bar{\beta}_1\Delta t}\boldsymbol{P}_n + \left(\frac{1}{\bar{\beta}_1} - 1\right)\dot{\boldsymbol{P}}_n\right) - \boldsymbol{F}^{P} = \boldsymbol{0}, \end{aligned} \tag{37}$$

where $\boldsymbol{\Psi}^{U}_{n+1}$ and $\boldsymbol{\Psi}^{P}_{n+1}$ denote the residuals associated with the updated displacements U_{n+1} and pressures P_{n+1}, respectively, and serve as measures of convergence in the nonlinear solution procedure. The coupled system of nonlinear equations is solved iteratively using a Newton–Raphson scheme. Correspondingly, at an arbitrary iteration i, the monolithic update scheme is defined by

$$\boldsymbol{J}^{i}_{n+1}\begin{bmatrix}\delta\boldsymbol{U}_n \\ \delta\boldsymbol{P}_n\end{bmatrix}^{i} = -\begin{bmatrix}\boldsymbol{\Psi}^{U}_{n+1} \\ \boldsymbol{\Psi}^{P}_{n+1}\end{bmatrix}^{i} \qquad \text{where} \qquad \begin{bmatrix}\delta\boldsymbol{U}_n \\ \delta\boldsymbol{P}_n\end{bmatrix}^{i} = \begin{bmatrix}\boldsymbol{U}_n \\ \boldsymbol{P}_n\end{bmatrix}^{i+1} - \begin{bmatrix}\boldsymbol{U}_n \\ \boldsymbol{P}_n\end{bmatrix}^{i}, \tag{38}$$

with $\delta\boldsymbol{U}_n$ and $\delta\boldsymbol{P}_n$ representing the additive updates to the displacement and pressure fields during iteration n, and the Jacobian matrix $\boldsymbol{J}^{i}_{n+1}$ given by

$$\boldsymbol{J}^{i}_{n+1} = \begin{bmatrix}\dfrac{\partial\boldsymbol{\Psi}^{U}_{n+1}}{\partial\boldsymbol{U}_{n+1}} & \dfrac{\partial\boldsymbol{\Psi}^{U}_{n+1}}{\partial\boldsymbol{P}_{n+1}} \\ \dfrac{\partial\boldsymbol{\Psi}^{P}_{n+1}}{\partial\boldsymbol{U}_{n+1}} & \dfrac{\partial\boldsymbol{\Psi}^{P}_{n+1}}{\partial\boldsymbol{P}_{n+1}}\end{bmatrix}^{i} = \begin{bmatrix}\dfrac{1}{\beta_1\Delta t^2}\boldsymbol{M} + \boldsymbol{K} & -\boldsymbol{G} \\ \dfrac{1}{\beta_1\Delta t^2}\boldsymbol{C} + \dfrac{\beta_2}{\beta_1\Delta t}\boldsymbol{G}^{\top} & \boldsymbol{H} + \dfrac{1}{\bar{\beta}_1\Delta t}\boldsymbol{S}\end{bmatrix}. \tag{39}$$

As evident from Eq. (39), the Jacobian matrix remains constant across both the iterations and time increments, i.e., $\boldsymbol{J}^{i}_{n+1} = \boldsymbol{J}$. This is due to the linearity of the underlying set of coupled differential equations, Eqs. (6) and (7), which are based on a linear hydro-elastic material behavior. Essentially, the nonlinearity of the set of algebraic Eqs. (36) and (37) may be fully ascribed to the use of an implicit time integration scheme.

When applying the present model for solving FEM problems characterized by a large number of elements, the computational time of the simulation may be significantly reduced by symmetrizing the Jacobian matrix (39), see also Mohammadnejad and Khoei (2013c,b), Khoei and Mortazavi (2020), Mortazavi et al. (2022). This can be done by (i) excluding the inertia matrix $\boldsymbol{C}$ from the Jacobian matrix (which can be safely ignored in the computation of $\boldsymbol{J}$, as its contribution is relatively small (Mohammadnejad and Khoei, 2013c; Khoei and Mortazavi, 2020)), and (ii) multiplying Eq. (36) by the value $-\beta_2/(\beta_1\Delta t)$. Hence, Eq. (38) becomes

$$\boldsymbol{J}^{\text{symm}}\begin{bmatrix}\delta\boldsymbol{U}_n \\ \delta\boldsymbol{P}_n\end{bmatrix}^{i} = -\begin{bmatrix}\left(-\dfrac{\beta_2}{\beta_1\Delta t}\right)\boldsymbol{\Psi}^{U}_{n+1} \\ \boldsymbol{\Psi}^{P}_{n+1}\end{bmatrix}^{i}, \tag{40}$$

with the symmetrized Jacobian given by

$$\boldsymbol{J}^{\text{symm}} = \begin{bmatrix}-\dfrac{\beta_2}{\beta_1\Delta t}\left(\dfrac{1}{\beta_1\Delta t^2}\boldsymbol{M} + \boldsymbol{K}\right) & \dfrac{\beta_2}{\beta_1\Delta t}\boldsymbol{G} \\ \text{symm.} & \boldsymbol{H} + \dfrac{1}{\bar{\beta}_1\Delta t}\boldsymbol{S}\end{bmatrix}. \tag{41}$$

The iterative update procedure, Eq. (38), is considered converged once the combined L_2-norm of the residuals $\boldsymbol{\Psi}^{U}_{n+1}$ and $\boldsymbol{\Psi}^{P}_{n+1}$ drops below a predetermined tolerance close to zero.

3. Numerical results

In this section we illustrate the accuracy and robustness of IGFEM for the hydro-mechanical analysis of saturated porous media with weak discontinuities in the solid displacement and fluid pressure fields. The

first example in Section 3.1 involves a saturated soil column consisting of two different sand materials that undergoes one-dimensional consolidation under vertical loading. The second example in Section 3.2 explores the two-dimensional consolidation behavior of a soil structure composed of two distinct sand layers under a vertical surface load. The third example in Section 3.3 simulates the injection of water into an underground reservoir composed of three different rock materials. Finally, in Section 3.4 the transient response of a horizontally layered soil with a sinusoidal material interface is considered to demonstrate IGFEM's ability to accurately capture complex, non-planar interfaces without requiring mesh alignment.

All examples are analyzed both with standard FEM using conformal finite elements at the material interface, and with IGFEM using nonconformal finite elements at the material interface. The FEM results serve as benchmark solutions for validating the outcomes obtained using the IGFEM method. The numerical results are computed by implementing the model formulation in Section 2 on the MATLAB numerical computing platform. The finite element meshes are constructed using four-node quadrilateral (Q4) elements with bilinear interpolation for both displacement and pressure fields, and utilizing 2×2 Gauss integration for each. In the IGFEM analysis, triangular integration elements are employed for the numerical integration over the area of enriched elements.

The standard $\boldsymbol{u}$–p formulation is known to exhibit numerical stability issues arising from violations of the Ladyzhenskaya–Babuška–Brezzi (LBB) condition, particularly in two limiting cases: (i) the undrained limit ($\boldsymbol{w} \to \boldsymbol{0}$), and (ii) the rigid skeleton limit ($\boldsymbol{u} \to \boldsymbol{0}$), see Lotfian and Sivaselvan (2018). In these regimes, the system behavior approaches that of incompressibility, making the choice of finite element spaces for displacement and pressure critical. The LBB condition provides a stability criterion that ensures proper coupling between these fields; failure to satisfy it can lead to checkerboard pressure patterns, locking, and poor convergence—phenomena commonly observed in standard equal-order interpolations of displacement and pressure. In this study, the material parameters and boundary conditions naturally lie sufficiently far from the limiting cases, which relaxes the incompressibility constraint and mitigates the strictness of the LBB condition. Under such conditions, stable and accurate solutions are obtained using bilinear interpolation for both displacement and pressure fields, with no evidence of spurious pressure oscillations or locking in the examples presented.

3.1. One-dimensional consolidation of a layered soil column

Consider the one-dimensional benchmark problem introduced by Khoei and Haghighat (2011), which involves a saturated soil column composed of two distinct sand materials, labeled "1" and "2", separated by a material interface at the mid-depth, see Fig. 4. The column consolidates under a time-dependent vertical load applied to its top surface. This problem enables an accurate comparison of the IGFEM results with both FEM results and the XFEM/GFEM results obtained by Khoei and Haghighat (2011). The geometry and the loading and boundary conditions of the problem are displayed in Fig. 4a. The Young's moduli of the two sand materials are $E_1 = 60 \times 10^6$ N/m^2 and $E_2 = 30 \times 10^6$ N/m^2, and the intrinsic permeabilities are $\kappa_1 = 1.02 \times 10^{-12}$ m^2 and $\kappa_2 = 1.02 \times 10^{-11}$ m^2. The remaining properties of the two soils are identical, with the Poisson's ratio as $\nu = 0.2$, the solid and fluid densities as $\rho_s = 2000$ kg/m^3 and $\rho_f = 1000$ kg/m^3, the bulk moduli of the solid and fluid phases as $K_s = 1.0 \times 10^{20}$ N/m^2 and $K_f = 2.1 \times 10^9$ N/m^2, Biot's coefficient as $\alpha = 1$, the porosity as $n = 0.3$, and the dynamic viscosity of the fluid phase (i.e., the groundwater) as $\mu = 10^{-3}$ N·s/m^2. For simplicity, gravitational loading effects are left out of consideration. All parameter values agree with those reported in Khoei and Haghighat (2011) for the same problem, where it should be noted that the above value for the bulk modulus K_s is artificially high, i.e., the sand particles are considered to be (almost) "ideally rigid". Nonetheless, additional simulations not presented here have shown that this assumption does not noticeably affect the numerical results; the grain bulk modulus of sandstone is typically relatively high, ranging from approximately 10 to 60 GPa (Qin et al., 2022), which validates the assumption of "ideally rigid" sand particles adopted in the analysis.

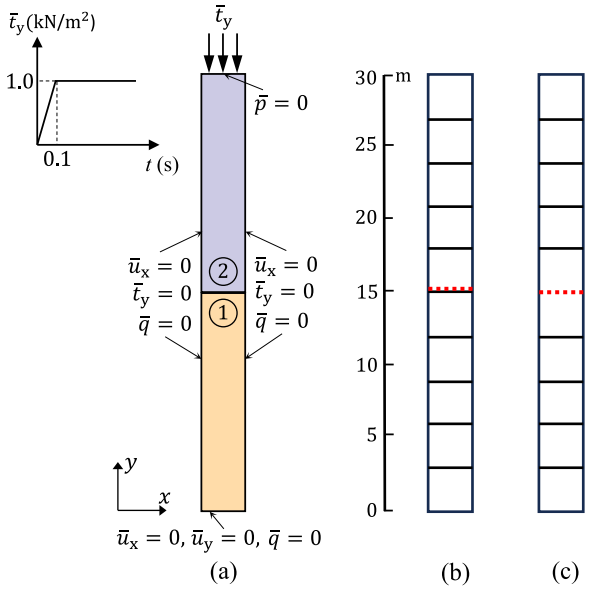

Fig. 4. A saturated soil column composed of two different sand materials, '1' and '2', separated by a material interface at mid-depth, undergoes consolidation under a time-dependent vertical load $\bar{t}_y$ applied at its top surface. (a) Load profile, geometry and boundary conditions. (b) FEM mesh with conformal finite elements at the material interface (indicated by a red dashed line). (c) IGFEM mesh with nonconformal finite elements at the material interface.

The initial displacements, velocities and excess pore pressure of the porous medium are prescribed to be zero. The vertical traction applied at the top surface of the soil column is increased linearly in time from $\bar{t}_y = 0$ to 1 kN/m^2 in 0.1 s, and subsequently remains constant. The bottom surface is rigidly supported, $\bar{u}_x = \bar{u}_y = 0$, and the horizontal displacement in the normal direction of the two lateral surfaces is zero, $\bar{u}_x = 0$. During loading, the pore pressure at the top surface is prescribed to be zero, $\bar{p} = 0$, while at the other three (impermeable) external boundaries the fluid flux is zero, $\bar{q} = 0$. Further, plane-strain conditions are assumed. The computational domain is discretized by 10 Q4 elements for the standard FEM analysis, and 9 Q4 elements for the IGFEM analysis, as respectively shown in Figs. 4b and 4c. The Newmark parameters used in the time integration scheme are $\beta_1 = \bar{\beta}_1 = 0.6$ and $\beta_2 = 0.605$, and the time increment increases logarithmically from $t = 0$ to $t = 200$ s in 1000 steps. The spatial discretization and computational settings are similar to those applied in Khoei and Haghighat (2011).

The time-dependent response of the soil column under the applied load is shown in Fig. 5 for the IGFEM method (red dashed line), the standard FEM method (blue solid line), and the XFEM/GFEM method as reported in Khoei and Haghighat (2011) (black dashed-dotted line). Here, Figs. 5a and 5b display the excess pore pressure p evaluated at $y = 9$ m and 27 m, respectively, and Figures 5c and 5d depict the vertical displacement u_y at $y = 24$ m and 30 m, respectively. The insets in Fig. 5 elucidate the initial transient responses from the IGFEM and standard FEM analyses, as evaluated between $t = 0.1$ s to $t = 1$ s. Since the initial transient response of the XFEM/GFEM simulation was not reported in detail by Khoei and Haghighat (2011), this result does not appear in the insets. Observe that the results computed with IGFEM are in excellent agreement with those calculated with standard FEM, both in the initial transient regime and over the complete time domain. Conversely, the XFEM/GFEM results reported by Khoei and Haghighat (2011) show some inaccuracy in both the pressure and

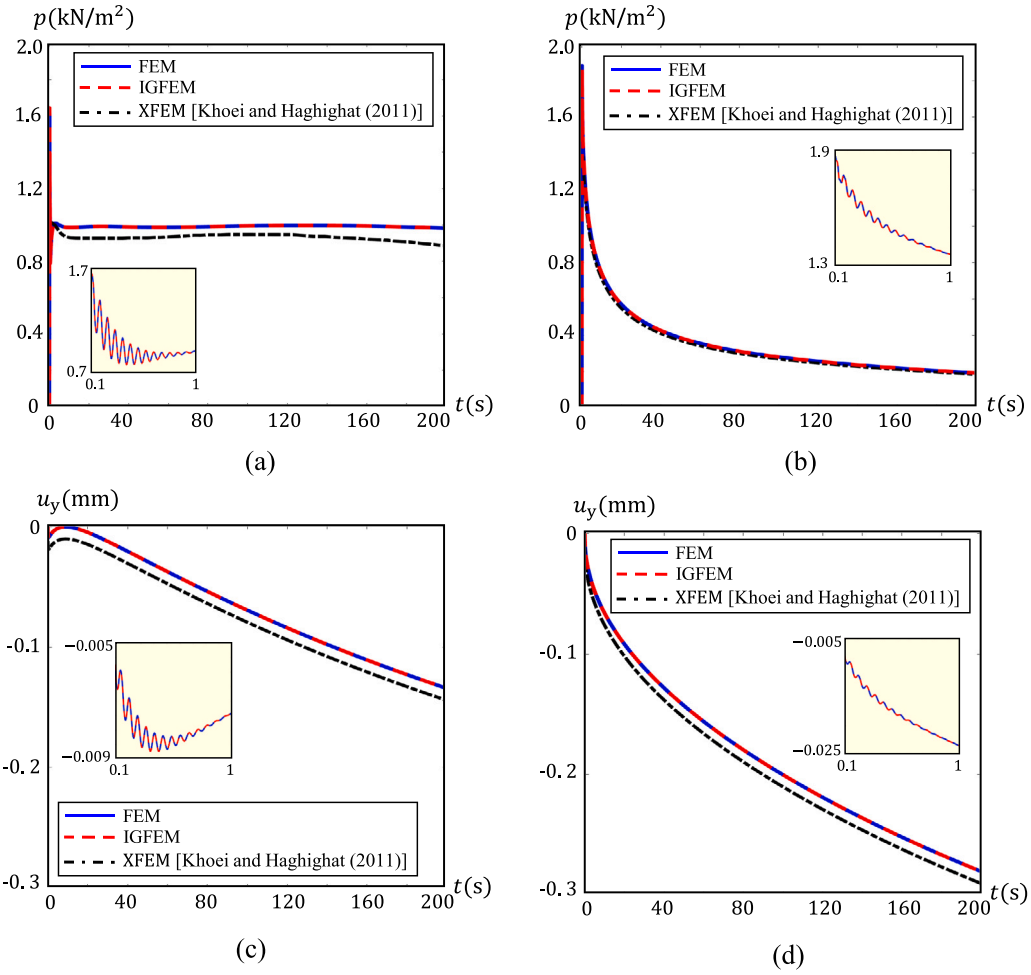

Fig. 5. Time-dependent responses for the consolidation problem depicted in Fig. 4, computed with the standard FEM model (blue solid line), the IGFEM model (red dashed line), and the XFEM/GFEM model presented in Khoei and Haghighat (2011) (black dashed-dotted line). (a) Excess pore pressure p at $y = 9$ m. (b) Excess pore pressure p at $y = 27$ m. (c) Vertical displacement u_y at $y = 24$ m. (d) Vertical displacement u_y at $y = 30$ m. The insets show in detail the initial, transient part of the response from $t = 0.1$ s to $t = 1$ s, computed with the standard FEM model (blue solid line) and IGFEM model (red dashed line).

displacement responses. A potential source of this inaccuracy could be the emergence of parasitic nonlinear terms in the spatial approximations of the primary variables within the linear blending elements, as discussed in Section 2.3. It should be noted that XFEM/GFEM results presented by Khoei and Haghighat (2011) shown in Fig. 5 serve as a reference only. As their formulation was not implemented within our computational framework, metrics such as convergence rates, matrix conditioning, and computational cost cannot be evaluated or directly compared with the IGFEM results.

The excess pore pressure p in the lower part of the structure ($y = 9$ m) remains nearly constant throughout most of the considered time period, see Fig. 5a, while the pore pressure in the upper part of the structure ($y = 27$ m) steadily tends to decrease to zero, see Fig. 5b. The faster dissipation of pore water in the upper part of the structure clearly is due to pore water leaving the structure at the top surface, at which the external pressure is prescribed to be zero. Fig. 5c shows that the magnitude of the vertical displacement u_y at $y = 24$ m initially slightly oscillates due to transient effects in the pore pressure, and after approximately 10 s increases monotonically in an almost linear fashion. The final displacement value of $u_y = -0.14$ mm reached after 200 s is half the magnitude of the final displacement value $u_y = -0.28$ mm observed at the upper surface $y = 30$ m, see Fig. 5d, illustrating the rapid decrease in displacement with depth.

Figs. 6a and 6b show the vertical displacement and pore pressure distributions, respectively, along the height of the column at $t = 200$ s. The results obtained using IGFEM demonstrate excellent agreement with those computed using standard FEM. A distinct change in the slope of both profiles is observed at the material interface located at $y = 15$ m, the mid-height of the soil column. While the vertical displacement remains continuous across the interface, its gradient changes abruptly (see Fig. 6a), indicating that the upper soil layer has a lower stiffness and therefore undergoes greater settlement. Similarly, the pore pressure profile is continuous but exhibits a noticeable kink at the interface (see Fig. 6b), which results from the contrast in intrinsic permeability between the two soil layers.

3.2. Two-dimensional consolidation of a horizontally stratified soil structure

The second problem concerns the two-dimensional consolidation behavior of a saturated, horizontally stratified soil structure subjected to a surface load and plane-strain conditions, see Fig. 7a. The practical benefit of this analysis lies in demonstrating that applying a surface load is essential for managing consolidation; it helps reduce future settlements and control construction timelines in a safe and cost-effective manner. As a proactive measure in geotechnical design, it directly impacts the performance and long-term durability of infrastructure built on soft or compressible soils. In the numerical problem, the soil structure has a vertical cross-section of $30 \times 30\,\text{m}^2$, which is composed of two horizontal sand layers separated by a material interface located

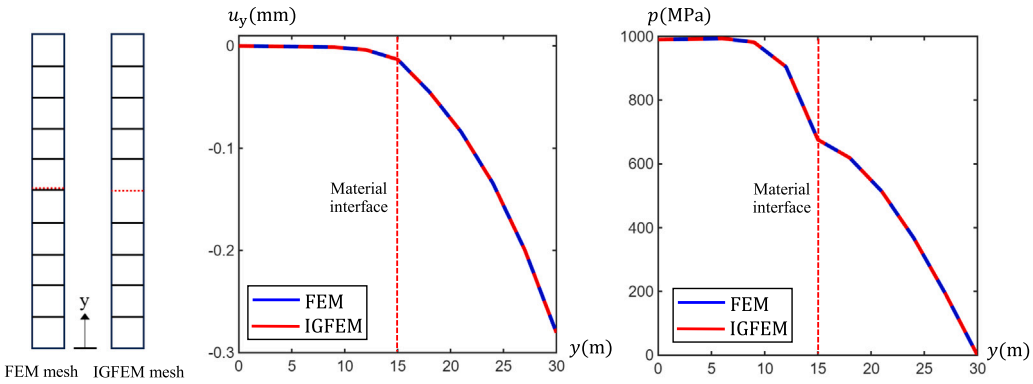

Fig. 6. Vertical displacement and pore pressure distributions along the column height at $t = 200\,\text{s}$, computed by the standard FEM model (blue solid line) and the IGFEM model (red dashed line). (a) Vertical displacement u_y. (b) Excess pore pressure p.

at $y = 24\,\text{m}$ from the bottom of the structure. The consolidation process occurs under the application of a time-dependent, vertical traction $\bar{t}_y$ applied at the upper surface over a horizontal distance of 6 m from the right boundary. The remaining part of the upper surface is modeled as traction-free and the pressure at the upper surface equals zero (thus referring to atmospheric pressure). Similar as for the previous problem, the bottom surface is rigidly supported, $\bar{u}_x = \bar{u}_y = 0$, and the normal displacement of the two lateral boundaries is set to zero, $\bar{u}_x = 0$. Furthermore, the flux is set to zero, $\bar{q} = 0$, at the two lateral surfaces and the bottom surface. The Newmark parameters used in the time integration scheme, as well as the material parameters, are taken the same as for the first problem presented in Section 3.1, except for the intrinsic permeabilities of the two soil materials; the permeabilities here have somewhat larger values, $\kappa_1 = 5 \times 10^{-11}\ \text{m}^2$ and $\kappa_2 = 10^{-10}\ \text{m}^2$, in order to more clearly highlight specific features of the time-dependent response during the consolidation process. The initial displacements, velocities, and excess pore pressure within the porous medium are set to zero. The traction at the top surface increases linearly from $\bar{t}_y = 0$ to $\bar{t}_y = 350\,\text{kN/m}^2$ in 1 s, and remains constant thereafter. The computational domain is discretized using a structured mesh of 729 Q4 elements for the standard FEM analysis, and 702 Q4 elements for the IGFEM analysis, as shown in Figs. 7b and 7c, respectively.

The spatial discretizations were chosen based on a mesh convergence study involving three structured FEM meshes of increasing resolution: a coarse mesh with 225 Q4 elements, an intermediate mesh with 729 Q4 elements, and a fine mesh containing 2916 Q4 elements, see Fig. 8. The time-dependent hydro-mechanical response is evaluated at Point A, located at $x = 27\,\text{m}, y = 21\,\text{m}$ within the structural domain (refer to Fig. 7a), and compared across the three mesh configurations. Fig. 9 presents the evolution of excess pore pressure p and vertical displacement u_y at Point A as functions of time. The insets in Fig. 9 elucidate the response between $t = 1\,\text{s}$ and $t = 5\,\text{s}$ (displayed on a logarithmic time scale). As shown, the coarse mesh exhibits small but noticeable deviations, particularly in the displacement response, relative to the intermediate and fine meshes. In contrast, the results from the intermediate and fine meshes are in excellent agreement, indicating mesh convergence. Based on this observation, the intermediate mesh is adopted for the final analysis, as it provides a favorable balance between accuracy and computational efficiency. In addition to spatial discretization, the impact of temporal resolution is investigated using the intermediate mesh. Three logarithmically increasing time-stepping schemes are considered over the simulated time interval $t \in [0, 200\,\text{s}]$: the first one with 500 time steps, the second one with 1000 time steps, and the third one with 1500 time steps. For all cases, the Newmark integration parameters are set to $\beta_1 = \bar{\beta}_1 = 0.6$ and $\beta_2 = 0.605$, ensuring consistent numerical damping and stability throughout the simulations. The corresponding time histories of excess pore pressure p and vertical displacement u_y at Point A are shown in Fig. 10. The response in the interval $t = 1\,\text{s}$ and $t = 5\,\text{s}$ is illustrated in greater detail in the insets of Fig. 9 (using a logarithmic time scale). The results obtained with 1000 and 1500 time steps show excellent agreement, whereas those with 500 time steps deviate slightly, indicating that temporal convergence is achieved at 1000 time steps. Accordingly, the more efficient scheme with 1000 time steps is employed in the final analysis.

Figs. 11a and 11b respectively illustrate the excess pore pressure p and vertical displacement u_y as a function of time for the IGFEM and FEM methods, evaluated at point A located at $x = 27\,\text{m}, y = 21\,\text{m}$, and at point B located at $x = 27\,\text{m}, y = 27\,\text{m}$, see Fig. 7a for the locations. Clearly, the pressure and displacement responses computed by the two methods are identical. The pore pressures at points A and B rise from zero to a peak value as the surface traction increases to its maximum. Once the surface traction reaches and remains at this maximum, the pore pressures at both points gradually decrease toward zero due to the consolidation of the soil structure. The pore pressure at point B exhibits greater variation than at point A, which is attributed to the higher permeability of soil layer 2 compared to soil layer 1. At about $t = 0.1\,\text{s}$ the vertical displacements at points A and B begin to increase from zero, where at around $t = 1\,\text{s}$, minor oscillatory transients appear, which result from mass inertia effects. These effects are triggered by a sudden peak in pore pressure as the applied surface traction reaches its maximum. As time progresses, the vertical displacements at points A and B increase further due to the reduction in pore pressure characterizing the consolidation process.

The overall distributions of the excess pore water pressure p and vertical displacement u_y are depicted at $t = 20\,\text{s}$ and $t = 200\,\text{s}$ in Figs. 12 and 13, respectively. At both evaluation times, the IGFEM and FEM simulation results agree exactly throughout the entire structure. The pore water pressure during consolidation develops from a non-uniform, high-pressure profile ($t = 20\,\text{s}$) to a low-pressure profile ($t = 200\,\text{s}$) that is uniform across the width of the structure. As can be concluded from Figs. 12a and 13a, the excess pore pressure tends to gradually approach zero across the entire structure as time further progresses (leading to completion of consolidation), where the displacement field stabilizes and becomes time-invariant, with its maximum value located beneath the applied surface load.

3.3. Water injection into a layered underground reservoir

The third problem considers water injection into an underground reservoir, see Fig. 14. This is a key area of study in porous media research (Monteagudo and Firoozabadi, 2004; Hoteit and Firoozabadi, 2008; Hajiabadi and Khoei, 2019; Mortazavi et al., 2022; Khoei et al., 2023a), where analyses like the one presented here may help to characterize reservoir properties, such as permeability, porosity, and heterogeneity, thereby supporting more informed decisions regarding well placement and production strategies. Additionally, examining changes

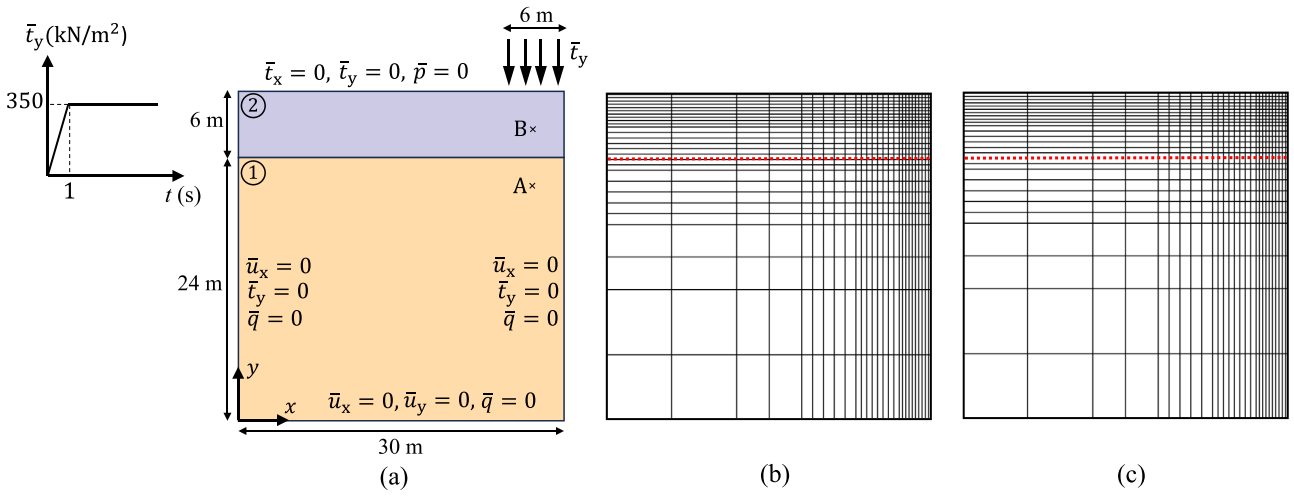

Fig. 7. A saturated stratified soil structure undergoes consolidation under a local, time-dependent vertical load $\bar{t}_y$ applied at its top surface. (a) Load profile, geometry and boundary conditions. (b) Structured FEM mesh with conformal finite elements at the material interface (indicated by a red dashed line). (c) Structured IGFEM mesh with nonconformal finite elements at the material interface.

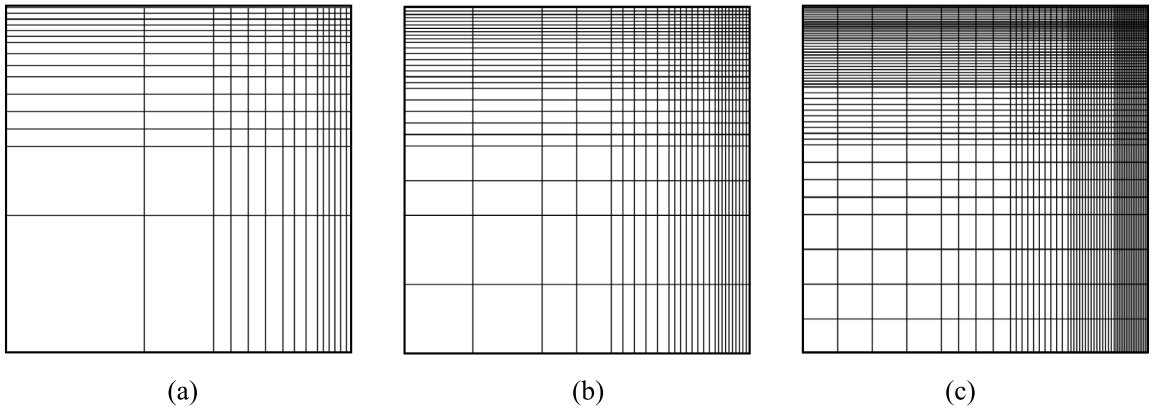

Fig. 8. Finite element meshes used in the mesh convergence study of the consolidation problem. (a) Coarse mesh with 225 Q4 elements. (b) Intermediate mesh with 729 Q4 elements. (c) Fine mesh with 2916 Q4 elements.

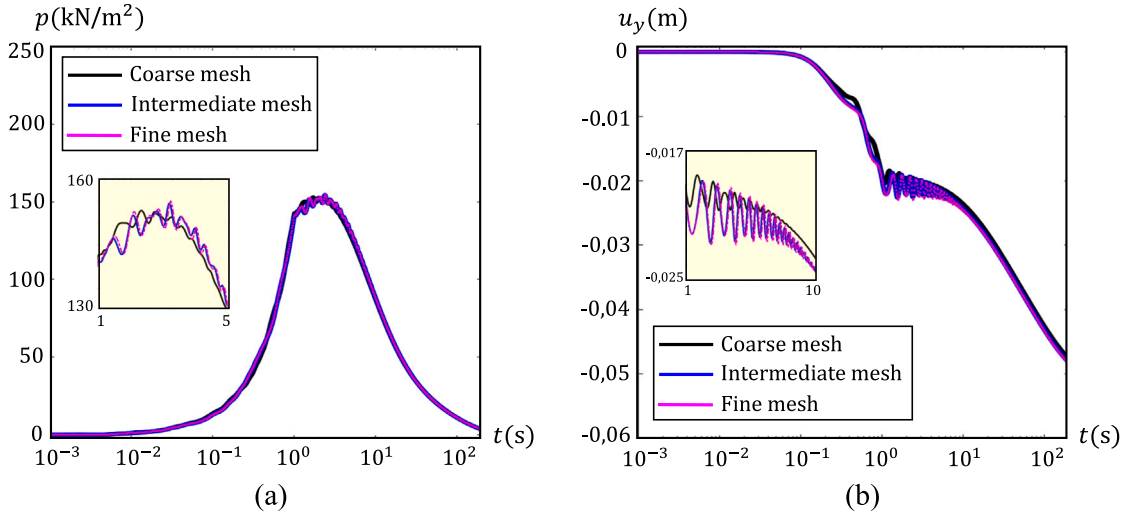

Fig. 9. Time-dependent FEM responses for the consolidation problem corresponding to the three mesh resolutions shown in Fig. 8, i.e., a coarse mesh (black solid line), an intermediate mesh (blue solid line) and a fine mesh (pink solid line). (a) Pore pressure p at Point A indicated in Fig. 7a. (b) Vertical displacement u_y at Point A indicated in Fig. 7a. The insets provide a detailed view of the response between $t = 1$ s and $t = 5$ s (depicted on a logarithmic time scale).

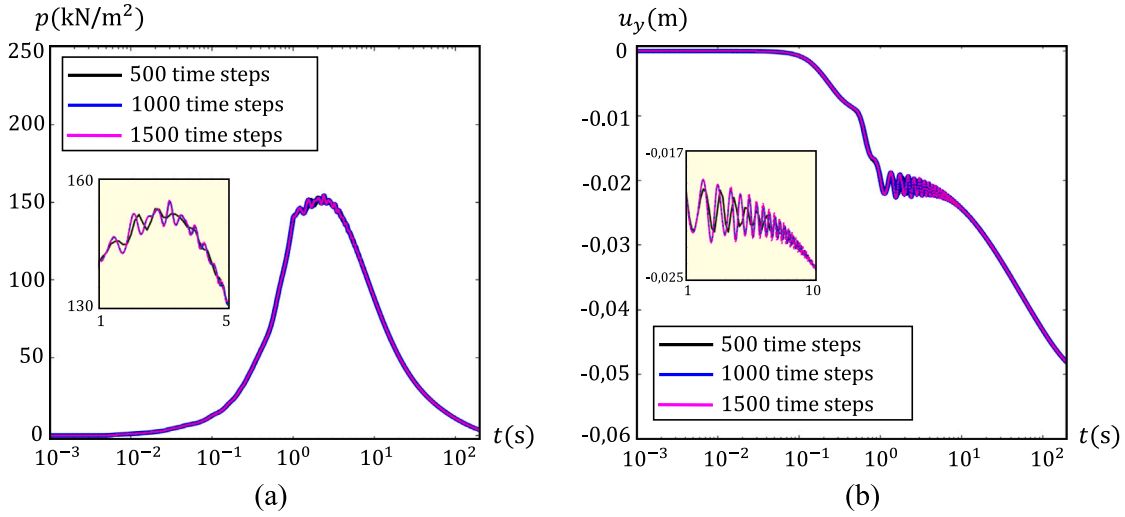

Fig. 10. Time-dependent FEM responses for the consolidation problem corresponding to temporal discretizations of 500 time steps (black solid line) 1000 time steps (blue solid line) and 1500 time steps (pink solid line). (a) Pore pressure p at Point A indicated in Fig. 7a. (b) Vertical displacement u_y at Point A indicated in Fig. 7a. The insets provide a detailed view of the response between $t = 1$ s and $t = 5$ s (depicted on a logarithmic time scale).

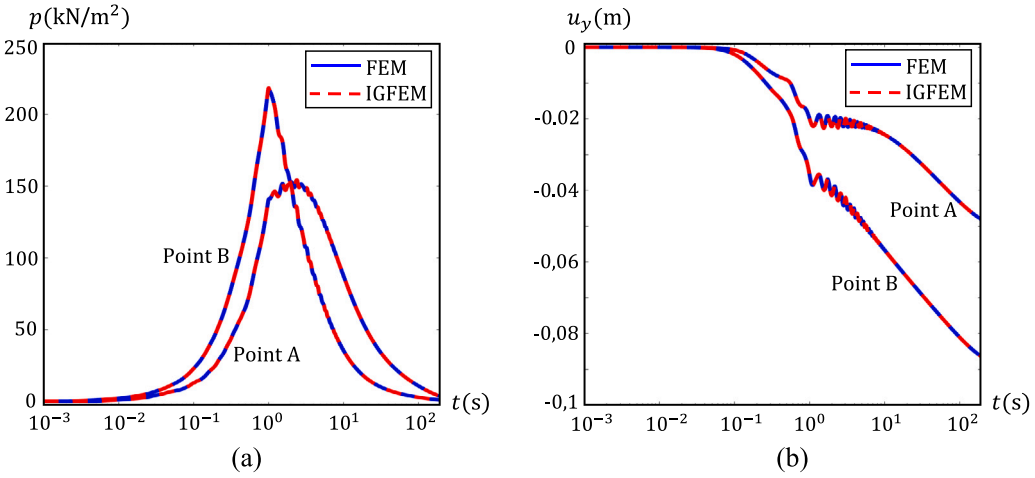

Fig. 11. Time-dependent responses for the consolidation problem depicted in Fig. 7, computed with the standard FEM model (blue solid line) and IGFEM model (red dashed line). (a) Excess pore pressure p at points A and B indicated in Fig. 7a. (b) Vertical displacement u_y at points A and B indicated in Fig. 7a.

in pore pressure resulting from water injection is essential for evaluating risks associated with induced seismicity, wellbore instability, and potential rock failure. In the numerical example, the reservoir has a horizontal cross-sectional area of $600 \times 600\,\mathrm{m}^2$ and is composed of three distinct, vertical rock layers, each 200 m thick, separated by two material interfaces, as illustrated in Figs. 14a and 14b. The Young's moduli of the rock materials are $E_1 = 4{\times}10^{10}\,\mathrm{N/m}^2$, $E_2 = 8{\times}10^{10}\,\mathrm{N/m}^2$, and $E_3 = 12 \times 10^{10}\,\mathrm{N/m}^2$, and the intrinsic permeabilities are $\kappa_1 = 1.97 \times 10^{-14}\,\mathrm{m}^2$ (20 mD), $\kappa_2 = 9.87 \times 10^{-15}\,\mathrm{m}^2$ (10 mD), and $\kappa_3 = 4.93 \times 10^{-15}\,\mathrm{m}^2$ (5 mD). The remaining material properties are similar to those of the first problem treated in Section 3.1.[1] The problem is simulated employing a 2D model that is subjected to plane-strain conditions in depth direction. The domain is discretized using a structured mesh of 900 Q4 elements for the standard FEM analysis, and 840 Q4 elements for the IGFEM analysis, as shown in Figs. 14c and 14d, respectively. Further mesh refinement was found to have no significant effect on the accuracy of the numerical results.

At the external boundaries the reservoir is rigidly supported, $\bar{u}_x = \bar{u}_y = 0$, and impermeable, $\bar{q} = 0$, see Fig. 14b. Water is injected at a constant rate of $1.25 \times 10^{-4}\,\mathrm{m}^3/\mathrm{s}$ (equivalent to 0.0001 PV/d) at the injection point located at the lower-left corner of the 2D geometry. At the production point located at the upper-right corner of the 2D geometry the water pressure is prescribed to be zero, $\bar{p} = 0$. The initial displacements, velocities and excess pore pressure within the reservoir are set to zero. A fixed time increment of $\Delta t = 3$ h is employed in the time-stepping scheme, with the Newmark parameters set to $\beta_1 = \bar{\beta}_1 = 0.6$ and $\beta_2 = 0.605$, which have been confirmed to produce converged results in time.

Fig. 15a illustrates the time evolution of fluid pressure p at the injection point (i.e., the injection pressure), while Fig. 15b presents the total horizontal displacement $u = \sqrt{u_x^2 + u_y^2}$ at the reservoir center over time, up to $t = 1500$ days of injection. Additionally, Fig. 15c shows the ratio of production flow rate to injection flow rate, $|Q_p/Q_i|$, and Fig. 15d depicts the ratio of cumulative water production volume to cumulative water injection volume, $|V_p/V_i|$, over the same period. Clearly, the results obtained using IGFEM are in exact agreement with

[1] Although Biot's coefficient α in Eq. (1) typically ranges between 1/3 and 2/3 for rock materials (Zienkiewicz et al., 1999), it is set to unity here for simplicity and to maintain consistency with the other two numerical examples analyzed.

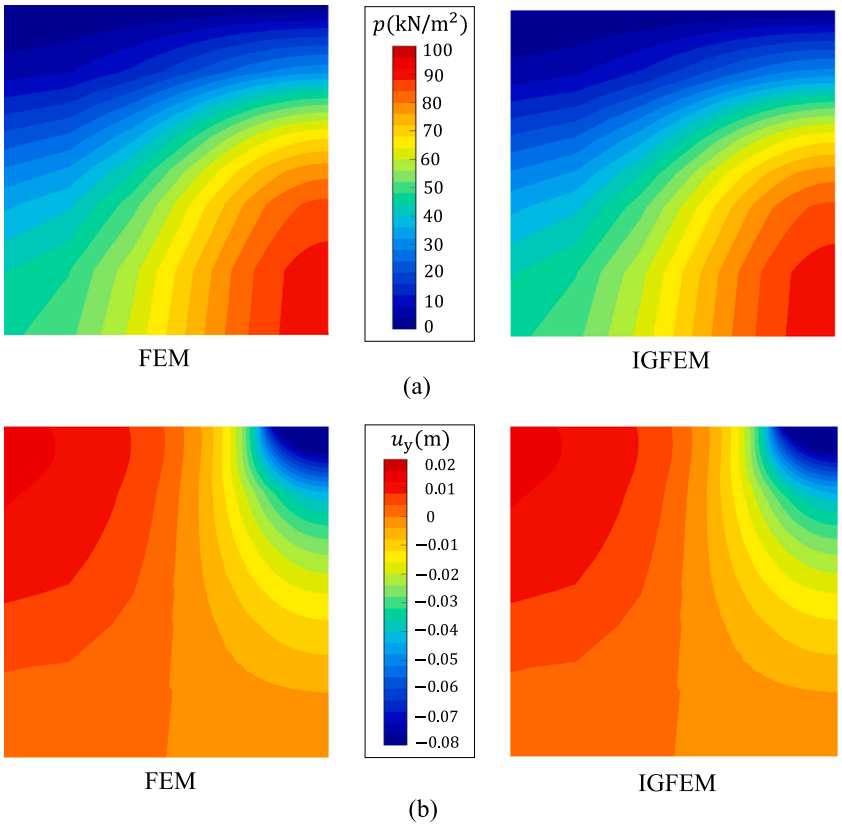

Fig. 12. Contour plots of field variables for the consolidation problem depicted in Fig. 7, computed with the standard FEM model (left) and the IGFEM model (right). (a) Excess pore pressure p across the structure at $t = 20$ s. (b) Vertical displacement u_y across the structure at $t = 20$ s.

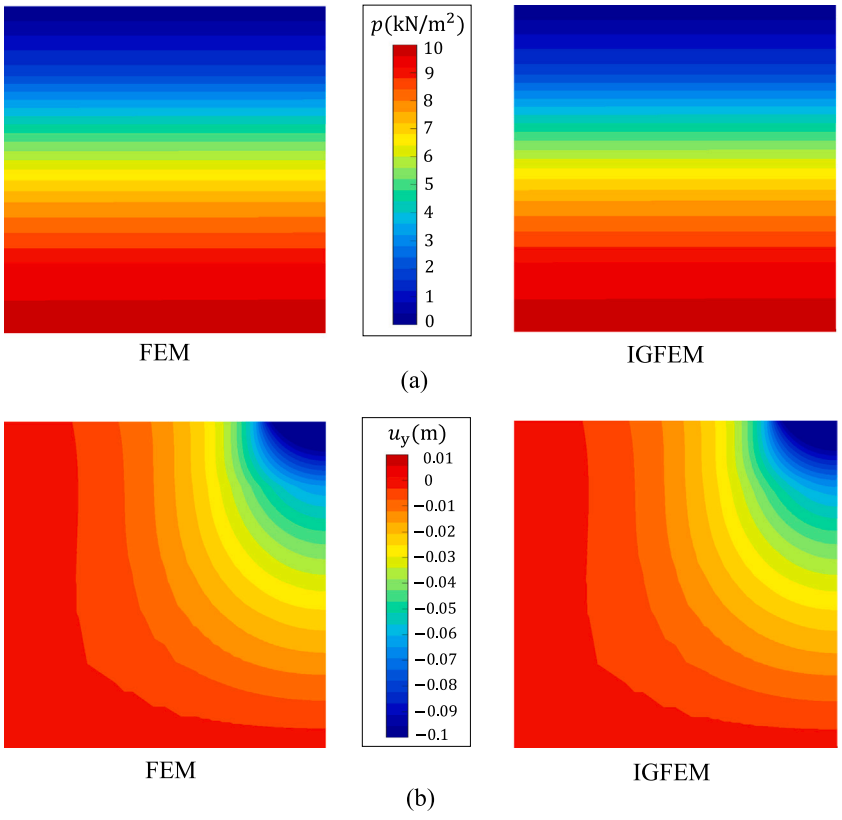

Fig. 13. Contour plots of field variables for the consolidation problem depicted in Fig. 7, computed with the standard FEM model (left) and the IGFEM model (right). (a) Excess pore pressure p across the structure at $t = 200$ s. (b) Vertical displacement u_y across the structure at $t = 200$ s.

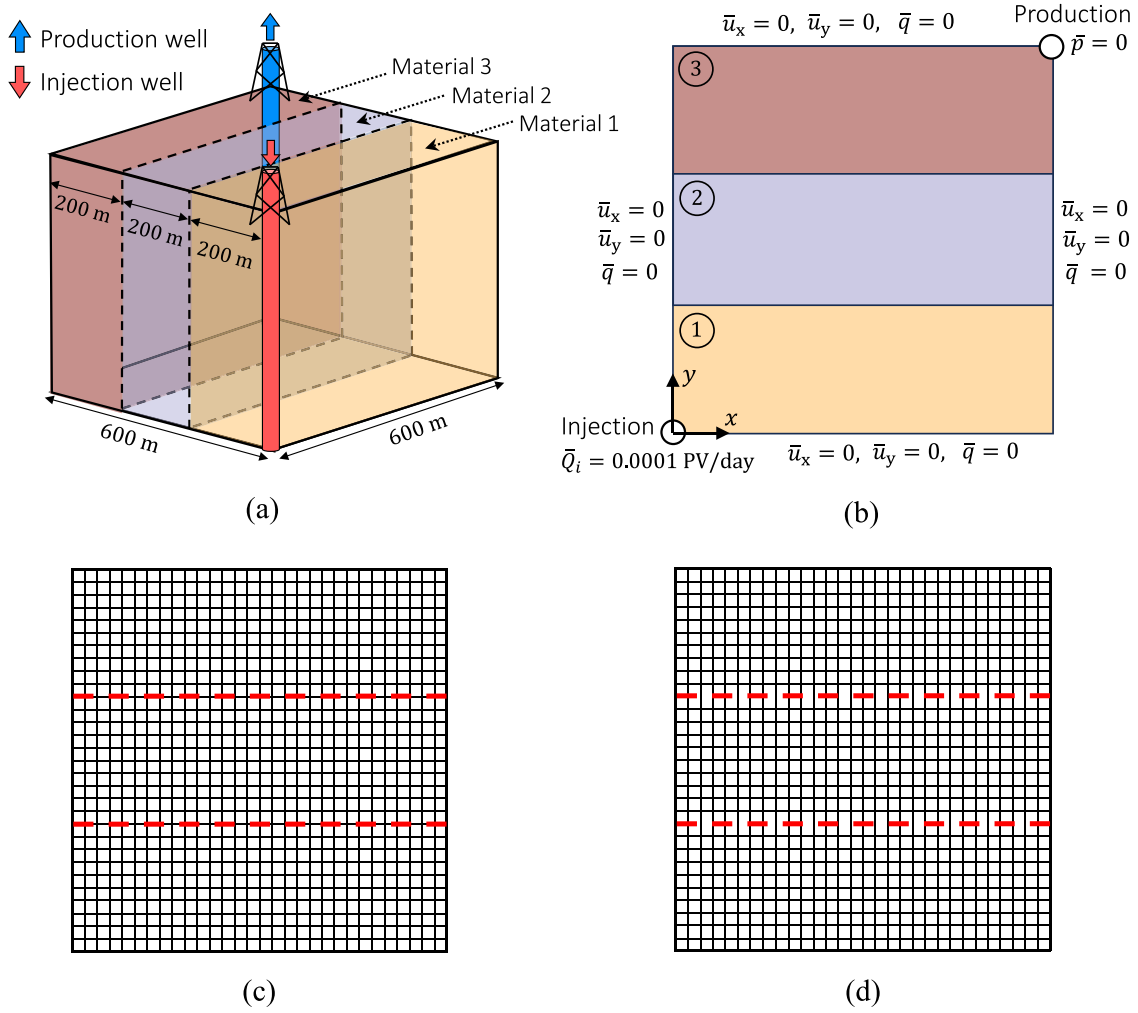

Fig. 14. Water injection into an underground reservoir consisting of three distinct, vertical rock layers. (a) Geometry of the reservoir with the locations of the injection and production wells. (b) Two-dimensional model geometry, with the points of water injection and production and the boundary conditions. (c) Structured FEM mesh with conformal finite elements at the two material interfaces (indicated by red dashed lines) (d) Structured IGFEM mesh with nonconformal finite elements at the two material interfaces.

those from the standard FEM approach. After an initial, transient jump in pore pressure caused by instantaneous flow initiation at the injection point, the pressure at the injection point steadily increases as pore water slowly migrates through the layered reservoir toward the production point. This leads to a growing horizontal displacement at the reservoir center, along with increasing ratios of production-to-injection flow rates and cumulative production-to-injection volumes. Over time, the flow field within the porous medium gradually approaches a steady state. At this stage, the injection-point pressure asymptotically stabilizes at slightly above 100 MPa, see Fig. 15a, the center point displacement reaches a final value of approximately 13 mm, see Fig. 15b, and the production-to-injection flow rate ratio approaches unity, see Fig. 15c. The cumulative production-to-injection volume ratio levels off at slightly above 0.8, see Fig. 15d, with the deviation from unity attributed to the volume of water retained within the porous medium.

Figs. 16a and 16b present the excess pore pressure and displacement profiles across the reservoir, respectively, evaluated at $t = 1500$ days, which approximately corresponds to the final, steady-state flow condition. The figures clearly indicate that the IGFEM and standard FEM models produce identical results. Observe further that the excess pore pressure steadily decreases from the injection point to the production point, with the maximum horizontal displacement approximately occurring at the center of the reservoir. Although the fluid pressure at the production point is prescribed as zero, it appears as 50 MPa in the contour plot, corresponding to the lower bound of the selected pressure range, which was chosen to optimize the visual representation of the pore pressure field.

3.4. Transient response of a horizontally layered soil with a sinusoidal material interface

The fourth problem is intended to demonstrate the accuracy and robustness of the proposed IGFEM formulation in the hydro-mechanical analysis of porous media with geometrically complex material interfaces. Specifically, this example highlights the effectiveness of IGFEM in situations where the standard finite element method would require complicated mesh alignment to accurately represent the interface geometry, whereas IGFEM accurately and efficiently solves the hydro-mechanical problem using a structured mesh that does not conform to the interface.

Fig. 17 illustrates a soil structure with a vertical cross-section of $25 \times 25\,\mathrm{m}^2$, consisting of two distinct sand layers separated by a sinusoidal material interface. The soil structure is modeled under plane-strain conditions, and is subjected to an impulsive vertical traction applied along the entire upper surface. The traction increases linearly from $\bar{t}_y = 0$ to $\bar{t}_y = 1500\,\mathrm{kN/m}^2$ over the first 1 s, and subsequently decreases linearly to $\bar{t}_y = 0$ during the interval from 1 to 2 s. The pore pressure at the upper boundary is set to zero, corresponding to atmospheric pressure. The bottom boundary is rigidly supported, with $\bar{u}_x = \bar{u}_y = 0$, while

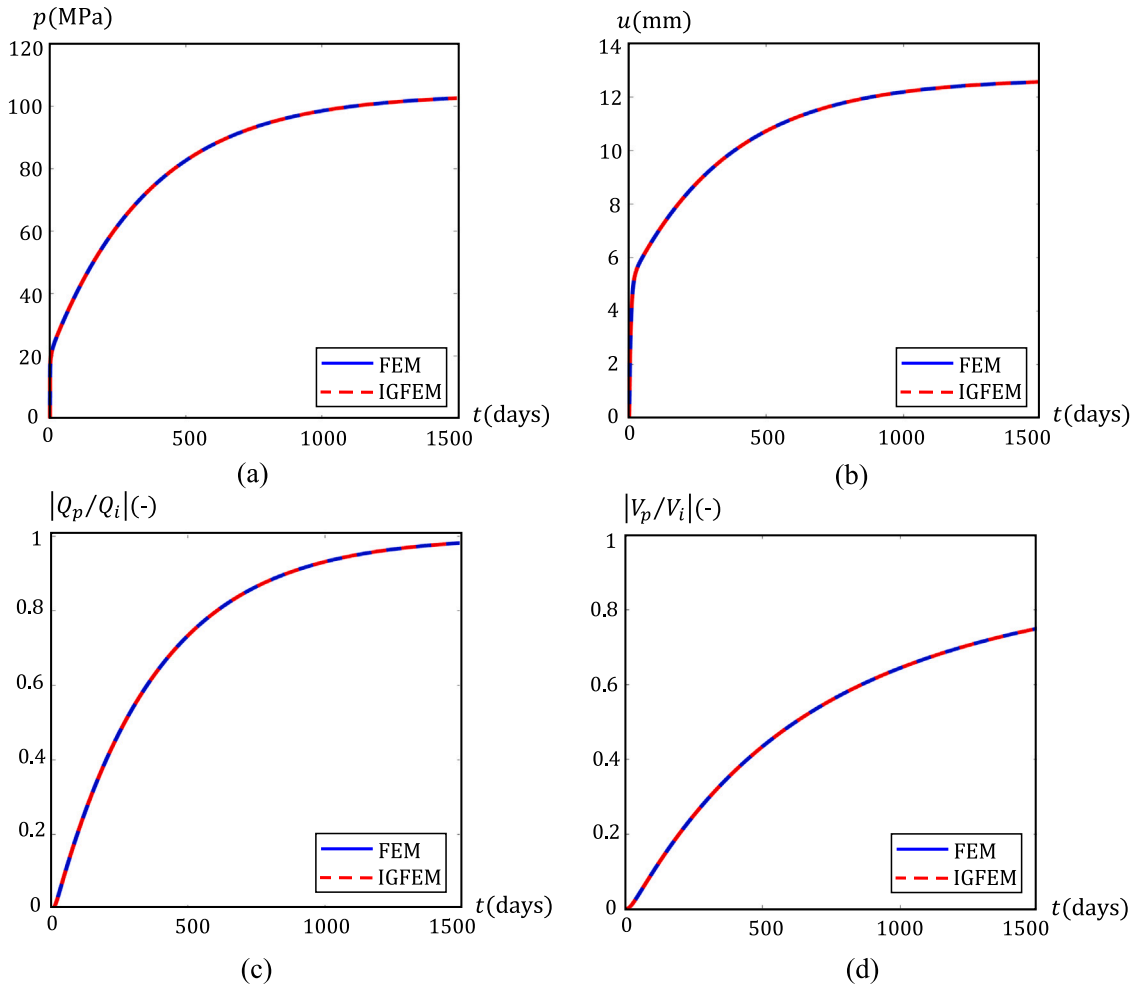

Fig. 15. Time-dependent responses for the problem of water injection into an underground reservoir depicted in Fig. 14, computed with the standard FEM model (blue solid line) and IGFEM model (red dashed line). (a) Fluid pressure p at the injection point. (b) Total horizontal displacement $u = \sqrt{u_x^2 + u_y^2}$ at the center of the reservoir. (c) Ratio of production flow rate to injection flow rate, $|Q_p/Q_i|$. (d) Ratio of cumulative water production volume to cumulative water injection volume, $|V_p/V_i|$.

the normal displacements at the two lateral boundaries are horizontally constrained by imposing $\bar{u}_x = 0$. In addition, the fluid flux is prescribed as zero, $\bar{q} = 0$, along both lateral boundaries and the bottom boundary. The Newmark parameters used in the time integration scheme, as well as the material parameters, are identical to those adopted in the first problem presented in Section 3.1, except for the Young's moduli and intrinsic permeabilities of the two sand layers. The Young's moduli are $E_1 = 3 \times 10^9$ N/m^2 and $E_2 = 3 \times 10^7$ N/m^2 (i.e., $E_1/E_2 = 100$), while the intrinsic permeabilities are $\kappa_1 = 10^{-12}, \text{m}^2$ and $\kappa_2 = 10^{-10}, \text{m}^2$ (i.e., $\kappa_1/\kappa_2 = 0.01$). The initial displacements, velocities, and excess pore pressures within the porous medium are set to zero. The time step increases logarithmically from $t = 0$ to $t = 50$ s over 1000 increments.

Fig. 18a presents the interface-fitted FEM mesh consisting of 1087 Q4 elements, in which the elements are locally refined in the vicinity of the sinusoidal material interface to accurately represent the interface geometry. Further mesh refinement was found to have a negligible effect on the accuracy of the FEM results. Fig. 18b shows the structured IGFEM mesh composed of 25×25 = 625 quadrilateral elements, in which the mesh does not conform to the material interface. The interface geometry causes some quadrilateral cut elements to be partitioned into two quadrilateral subdomains (Fig. 18d), while others are divided into a triangular and a pentagonal subdomain (Fig. 18c). The first case can be treated by modeling each quadrilateral subdomain with a quadrilateral child element with bilinear shape functions, as described in detail in Section 2.3 and illustrated in Fig. 3. However, when the interface partitions a quadrilateral parent element into a triangular and a pentagonal subdomain, an additional treatment is required to ensure that the IGFEM approximation retains optimal accuracy.

To this end, the quadrilateral parent element is subdivided into four triangular integration elements, as illustrated in Fig. 18c. Note that starting from the Lagrange interpolation of the quadrilateral parent element, the use of 3-node triangular integration elements for the evaluation of enrichment functions does not achieve optimal accuracy. This is because enrichment functions constructed with linear triangular elements do not contain the bilinear term present in the interpolation of the quadrilateral parent element. To address this issue, the approach proposed by Aragón et al. (2020) is adopted, in which the polynomial order of the enrichment functions is increased by employing 6-node quadratic triangular integration elements. As illustrated in Fig. 18c, the quadratic enrichment formulation introduces additional enriched nodes at the midpoints of the edges of the four triangular integration elements, indicated by red solid circles. Consequently, the loss of accuracy associated with linear enrichments based on 3-node integration elements is compensated by employing quadratic enrichments based on 6-node integration elements, see Appendix for further details.

Figs. 19a and 19b present the excess pore pressure p and vertical displacement u_y as functions of time (shown on a logarithmic time scale) at Points A ($x = 12.5\,\text{m}, y = 17\,\text{m}$) and B ($x = 12.5\,\text{m}, y = 23\,\text{m}$),

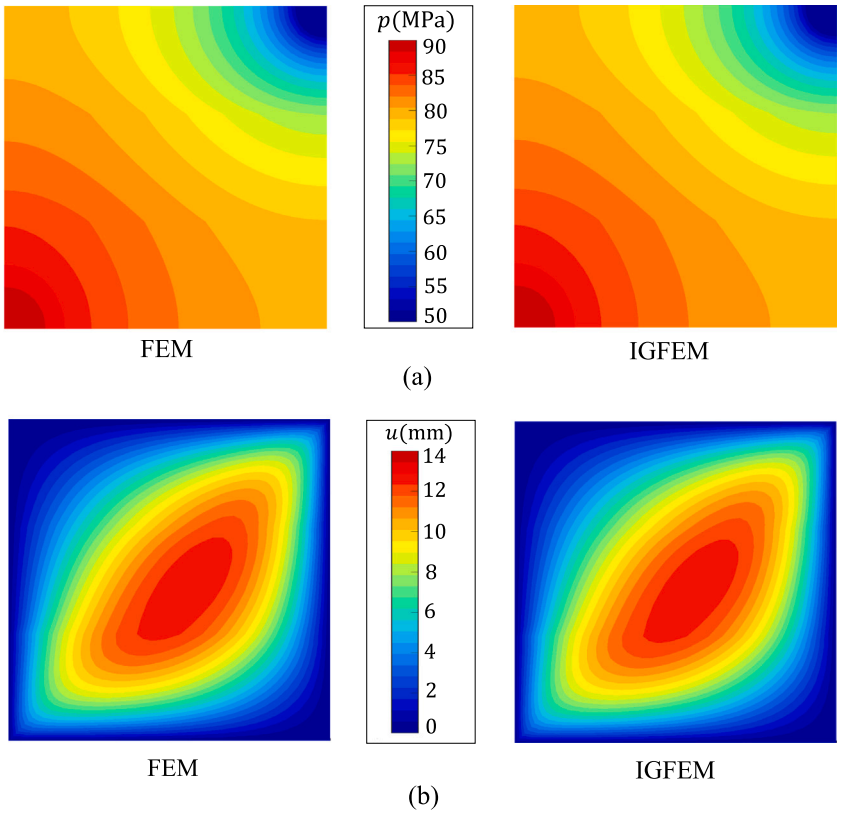

Fig. 16. Contour plots of field variables for the problem of water injection into an underground reservoir depicted in Fig. 14, computed with the standard FEM model (left) and the IGFEM model (right). (a) Excess pore pressure p across the structure at $t = 1500$ days. (b) Total horizontal displacement $u = \sqrt{u_x^2 + u_y^2}$ across the structure at $t = 1500$ days.

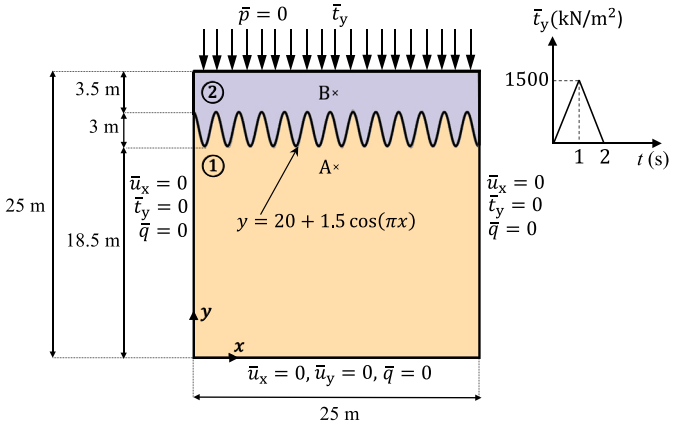

Fig. 17. Load profile, geometry and boundary conditions for a soil structure composed of two sand layers separated by a sinusoidal material interface.

respectively, see Fig. 17 for their locations. The responses are computed using both FEM and IGFEM, and the two methods show excellent agreement. During the loading phase ($0 < t < 1$ s), the impulsive traction generates significant positive excess pore pressure at both points, reaching its maximum approximately when the applied traction peaks at $t = 1$ s (Fig. 19a). This behavior reflects the nearly undrained response of the medium during rapid loading, where compression of the porous skeleton locally generates pore pressure while fluid drainage remains limited. During the unloading stage ($1 < t < 2$ s), the reduction of the external load causes a rapid decrease in pore pressure at Points A and B, eventually reaching a negative minimum. This negative pressure results from the elastic rebound of the solid skeleton, which temporarily expands the pore space faster than fluid can flow in to equilibrate the pressure. After unloading, the pore pressure gradually dissipates toward zero as the system approaches hydro-mechanical equilibrium. Because the bottom layer has lower permeability than the upper layer, the magnitude of the excess pore pressure at Point A is smaller than at Point B. Fig. 19b shows that the vertical displacement at both points increases during loading and gradually returns to zero after unloading. Due to the strong stiffness contrast between the two soil layers ($E_1/E_2 = 100$), most of the deformation occurs in the softer upper layer. Consequently, Point B, located in the upper layer, experiences a larger vertical displacement than Point A in the much stiffer lower layer.

Figs. 20a and 20b illustrate the contour plots of the excess pore water pressure p and the vertical displacement u_y, respectively, at the end of the unloading phase, $t = 2$ s. It can be observed that the FEM and IGFEM simulations are in excellent agreement for both the pressure and displacement fields throughout the entire domain. The pressure contours indicate that the negative excess pore pressures, generated by the rapid unloading and the delayed redistribution of pore fluid within the soil skeleton, are most pronounced in the upper region of the domain. Furthermore, the displacement contours demonstrate that the displacement magnitude decreases with depth, with most of the deformation occurring in the softer upper layer. The sinusoidal shape of the material interface further leads to spatial variations in both pressure and displacement along the interface, reflecting the local differences in stiffness and permeability between the two sand layers.

4. Summary and concluding remarks

In this paper we introduced the Interface-enriched Generalized Finite Element Method (IGFEM) for solving the fully coupled hydro-mechanical equations that govern deformable, saturated porous media

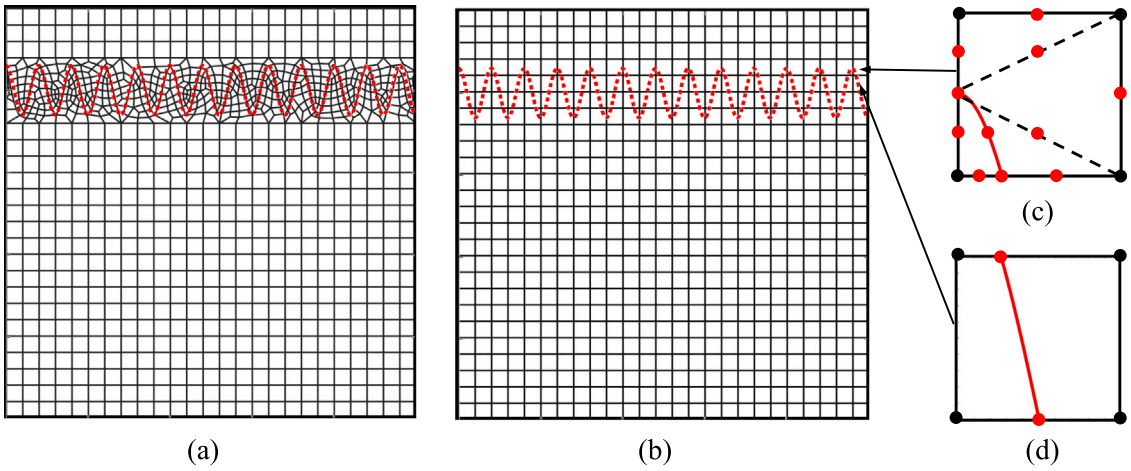

Fig. 18. FEM and IGFEM discretizations generated for the soil structure with a sinusoidal material interface shown in Fig. 17. (a) Conformal FEM mesh with local refinement around the sinusoidal material interface (red dashed line). (b) Structured IGFEM mesh with nonconformal finite elements at the material interface. (c) A quadrilateral parent element is split into one triangular and one pentagonal subdomain. The parent element is partitioned into four 6-node triangular integration elements with quadratic enrichment; additional enriched nodes are added at the edge centers. (d) A quadrilateral parent element is divided into two quadrilateral child elements. In (c) and (d), black and red solid circles represent standard and enriched nodes, respectively.

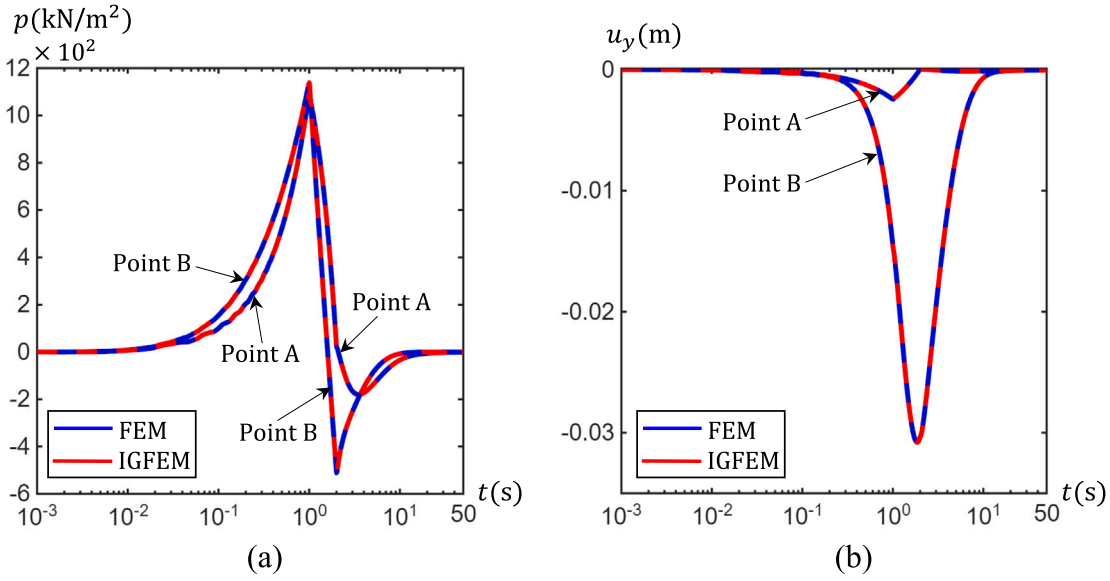

Fig. 19. Time-dependent responses of the soil structure with a sinusoidal material interface shown in Fig. 17, computed using the standard FEM model (blue solid line) and the IGFEM model (red dashed line). (a) Excess pore pressure p at points A and B, as indicated in Fig. 17. (b) Vertical displacement u_y at points A and B, as indicated in Fig. 17.

consisting of piecewise homogeneous phases. The coherent interfaces between the distinct, perfectly bonded homogeneous phases introduce weak discontinuities in both the solid-phase displacement and the fluid-phase pressure fields. In standard FEM, accurately representing these gradient discontinuities requires element edges to align with the interface, since misaligned elements cannot naturally reproduce the jumps in the derivatives of the primary variables. IGFEM overcomes this restriction by enriching the approximation space in cut elements—elements intersected by the material interface—with functions that reproduce the kinematics of weak discontinuities, enabling an accurate representation of gradient jumps without requiring the mesh to conform to the interface. The governing equations of the coupled hydro-mechanical analysis, which include the linear momentum balance equation and the storage equation of the saturated porous medium, are spatially discretized using IGFEM. The temporal discretization is subsequently carried out employing the generalized Newmark method. The resulting coupled system of equations is iteratively solved using a monolithic update scheme based on the Newton–Raphson method.

A key advantage of IGFEM is that it allows material interfaces to intersect elements *arbitrarily*, without requiring mesh conformity. This flexibility is realized by incorporating enrichment functions into the approximation space of cut elements. For numerical integration, these cut elements are further subdivided into integration elements using Lagrangian shape functions, which are then used to compute the local element contributions efficiently. Notably, the integration mesh may also be treated as a standard FEM mesh, with cut parent elements replaced locally by linear triangles. This approach essentially forms the

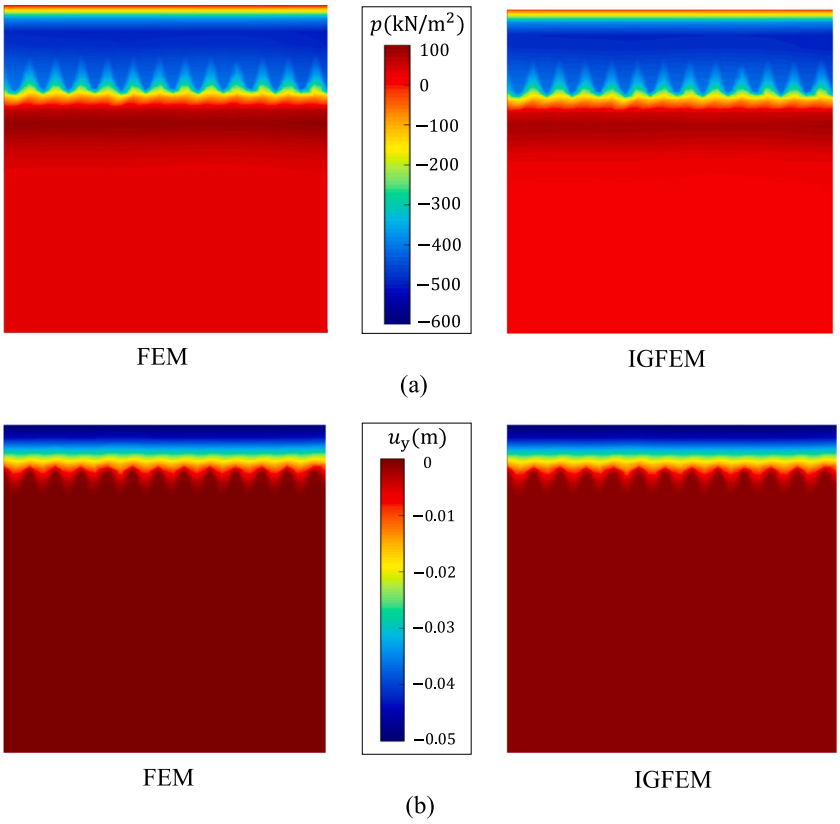

Fig. 20. Contour plots of field variables for the soil structure with a sinusoidal material interface depicted in Fig. 17, computed with the standard FEM model (left) and the IGFEM model (right). (a) Excess pore pressure p at $t = 2$ s. (b) Vertical displacement u_y at $t = 2$ s.

foundation of the Conformal Decomposition FEM (CD-FEM) of Noble et al. (2010). The key distinction is that IGFEM constructs the discrete space hierarchically: the standard FEM basis remains unchanged and enrichment functions are added on top. Although this compromises the partition-of-unity property in cut elements, the two formulations span the same linear space; consequently, IGFEM and CD-FEM yield identical solutions. In both approaches, however, sliver (geometrically degenerated) elements may lead to ill-conditioning. CD-FEM addresses this through preconditioning, whereas IGFEM, besides allowing preconditioning, offers an additional remedy: the enrichment functions can be scaled as interfaces approach mesh nodes, thereby preserving stability without modifying the underlying mesh (Aragón et al., 2020).

Compared with other enriched finite element methods, such as XFEM/GFEM, IGFEM employs a distinct enrichment strategy in which the enrichment functions are tied to nodes inserted directly along the discontinuity, rather than to the standard mesh nodes. As a result, the enrichment functions in IGFEM vanish identically in blending elements, i.e., in elements adjacent to cut elements, thereby avoiding the parasitic terms that can degrade accuracy and reduce convergence rates. Dealing with such artifacts in XFEM/GFEM requires either higher-oder approximations or modified enrichment functions that *cancel out* parasitic terms, as explained by Aragón et al. (2010). Ill-conditioning caused by interfaces passing arbitrarily close to mesh nodes arises in both XFEM/GFEM and IGFEM. In XFEM/GFEM, this issue is addressed by Stable GFEM (SGFEM) and Strongly Stable GFEM (SSGFEM) formulations (Kergrene et al., 2016; Zhang et al., 2020), which modify the enrichment functions to reduce their adverse impact on system conditioning. In contrast, IGFEM offers a considerably simpler remedy: stability can be achieved either by a simple Jacobi-like diagonal preconditioner or by scaling the enrichment functions as interfaces approach mesh nodes (Aragón et al., 2020). In both cases, the condition number scales with the mesh size h as $\mathcal{O}\left(h^{-2}\right)$, matching the behavior of standard FEM on fitted meshes. With regard to accuracy, IGFEM achieves the same convergence rates as standard FEM on geometry-fitted meshes (Soghrati et al., 2012; van den Boom et al., 2019), which are optimal for problems without singularities. XFEM/GFEM can also recover optimal convergence in the presence of singularities, provided that the approximation is enriched with appropriate problem-specific functions (Aragón and Duarte, 2023). Compared to standard FEM, both IGFEM and XFEM/GFEM incur only a minor CPU overhead, since interface-enriched DOFs form a small fraction of the total. As the mesh is refined, computational cost is dominated asymptotically by the standard bulk DOFs.

The four numerical examples presented in this paper demonstrate the effectiveness of the current IGFEM formulation and its applicability to solving practical geotechnical problems. Specifically, the examples considered are: (i) One-dimensional consolidation of a layered soil column; (ii) Two-dimensional consolidation of a horizontally stratified soil structure; (iii) Water injection into a layered underground reservoir; (iv) Transient response of a horizontally layered soil with a sinusoidal material interface. The excellent agreement between IGFEM results and those obtained using standard FEM with conformal meshes in all four examples validates the accuracy and robustness of the proposed approach. Converged solutions in both space and time are demonstrated through systematic refinement of the mesh and time-step size, respectively. In the first example, the numerical results are also compared with those reported by Khoei and Haghighat (2011) using XFEM/GFEM. While IGFEM provides an accurate solution, the XFEM/GEM approach exhibits noticeable errors in the displacement and pressure fields. A potential source of the inaccuracies observed in XFEM/GFEM is the parasitic nonlinear terms that arise in blending elements. IGFEM avoids this issue, as discussed above, because the enrichment functions vanish exactly in these elements. In addition, the fourth example, which involves a sinusoidal material interface, demonstrates

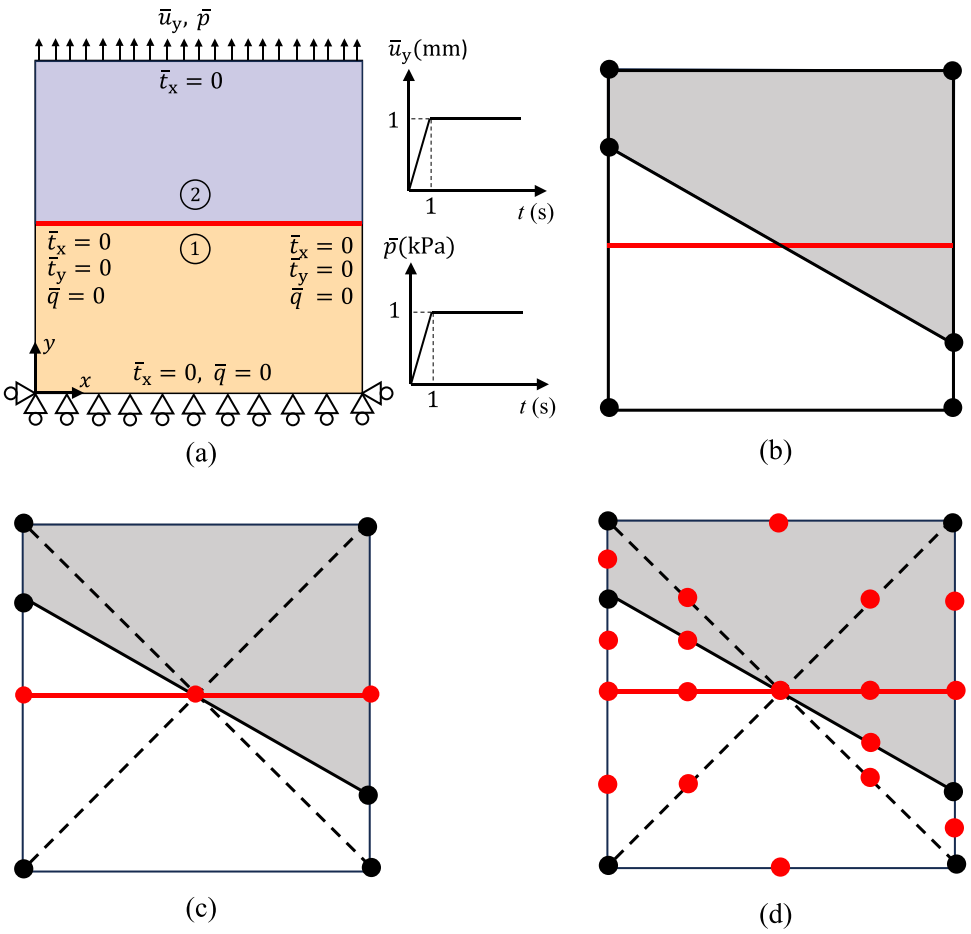

Fig. 21. IGFEM patch test for a bimaterial porous medium using linear versus quadratic enrichment functions. (a) Geometry, loading and boundary conditions. (b) Two quadrilateral parent elements (shown in white and gray), each divided by a material interface (red solid line) into a triangular and a pentagonal subdomain. (c) Subdivision of each of the two quadrilateral parent elements into four triangular integration elements with *linear* enrichments, with black and red solid circles representing standard and enriched nodes, respectively. (d) Subdivision of each of the two quadrilateral parent elements into four triangular integration elements with *quadratic* enrichments, with additional enriched nodes located at the centers of the edges.

IGFEM's ability to accurately capture complex, non-planar interfaces without requiring mesh alignment, further highlighting the method's flexibility and robustness for practical hydro-mechanical analyses of porous media with geometrically intricate boundaries.

The model formulation and results presented in this paper provide promising directions for future research on IGFEM modeling of saturated porous media with material interfaces. For instance, the IGFEM approach can be extended to perform thermo-hydro-mechanical (THM) analyses of porous media with embedded material interfaces. In such problems, not only the solid displacement and fluid pressure fields, but also the temperature field may exhibit weak discontinuities across material interfaces. Another potential avenue for future work could be to extend the present IGFEM formulation by incorporating the modeling of strong discontinuities in accordance with the Discontinuity-Enriched Finite Element Method (DE-FEM) (Aragón and Simone, 2017), thereby enabling the analysis of fractured heterogeneous porous media or its fracture propagation following Zhang et al. (2025).

CRediT authorship contribution statement

Pouriya Pirmoradi: Writing – review & editing, Writing – original draft, Validation, Software, Methodology, Formal analysis, Data curation, Conceptualization. **Alejandro M. Aragón:** Writing – review & editing, Writing – original draft, Validation, Methodology, Conceptualization. **Payam Poorsolhjouy:** Writing – review & editing, Validation, Supervision, Project administration, Conceptualization. **Akke S.J. Suiker:** Writing – review & editing, Writing – original draft, Validation, Supervision, Project administration, Funding acquisition, Conceptualization.

Declaration of competing interest

The authors declare that they have no known competing financial interests or personal relationships that could have appeared to influence the work reported in this paper.

Acknowledgments

The authors gratefully acknowledge the financial support provided by the "Sectorplan Techniek 2019". A.S.J.S. is grateful for the financial support provided by the Eindhoven Institute for Renewable Energy Systems (EIRES).

Appendix. IGFEM patch test for a bimaterial porous medium

In this appendix, a patch test is performed for a bimaterial porous medium to verify that the proposed formulation can accurately reproduce a bilinear solution field when a quadrilateral cut element is divided by the material interface into triangular and pentagonal subdomains. In principle, a material interface may intersect a quadrilateral parent element in three possible ways: (i) splitting it into two quadrilateral subdomains, (ii) splitting it into a triangular and a pentagonal

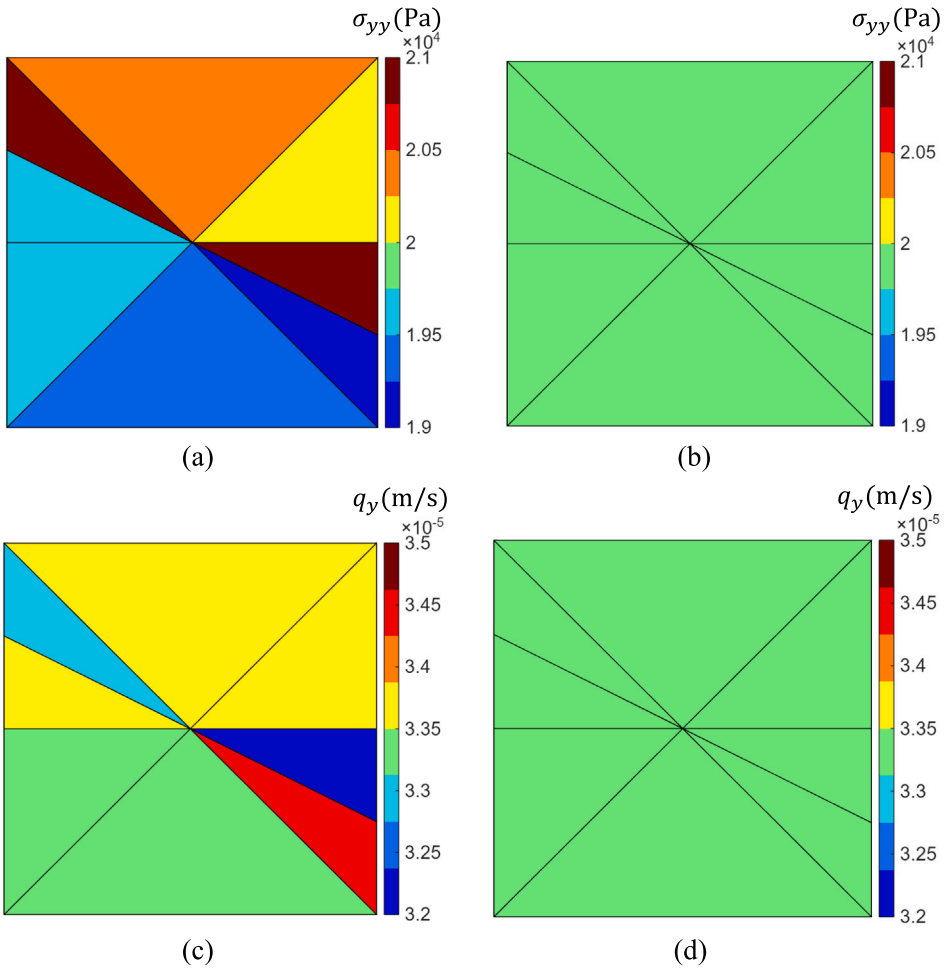

Fig. 22. Results of the IGFEM patch test using element formulations with *linear* and *quadratic* enrichments, as illustrated in Figs. 21c and 21d, respectively. (a) Normal stress σ_{yy} for triangular integration elements with *linear* enrichments. (b) Normal stress σ_{yy} for triangular integration elements with *quadratic* enrichments. (c) Flux q_y for triangular integration elements with *linear* enrichments. (d) Flux q_y for triangular integration elements with *quadratic* enrichments. Discretizations with linear enrichments, as shown in Figs. 22a and c, fail the patch test, whereas those with quadratic enrichments, as shown in Figs. 22b and d, successfully pass by reproducing constant stress and flux fields.

subdomain, and (iii) splitting it into two triangular subdomains. The first case can be treated straightforwardly by dividing the quadrilateral parent element into two quadrilateral child elements with bilinear shape functions, as demonstrated in the numerical examples presented in Sections 3.1 to 3.3. The remaining cases require additional treatment to ensure that the IGFEM approximation satisfies the patch test and achieves optimal accuracy. Hence, a numerical patch test is conducted for the coupled hydro-mechanical IGFEM formulation corresponding to case (ii), which, together with case (i), is the element formulation used to solve the fourth numerical example presented in Section 3.4.

The patch test is performed on a 2×2 m^2 porous medium composed of two different materials separated by a straight interface, as shown in Fig. 21a. The bottom edge of the medium is fixed in the y-direction ($\bar{u}_y = 0$), and the left and right corners of this edge are additionally constrained in the x-direction ($\bar{u}_x = 0$). Zero flux is prescribed along the side edges and the bottom edge ($\bar{q} = 0$). In addition, both the horizontal and vertical tractions at the left and right edges vanish ($\bar{t}_x = 0$, $\bar{t}_y = 0$). A displacement field is prescribed at the top edge, increasing linearly from $\bar{u}_y = 0$ to $\bar{u}_y = 1$ mm over 1 s, and maintained constant thereafter. Similarly, the pore pressure at the top edge is increased from $\bar{p} = 0$ to $\bar{p} = 1$ kPa over 1 s and kept constant thereafter. The initial displacement, velocity, and fluid pressure fields within the medium are all zero. Material properties and Newmark parameters are taken to be the same as those used in Section 3.2. The only exception is the Poisson's ratio, which is taken as zero for both materials, $\nu = 0$. This eliminates lateral deformation induced by Poisson coupling and avoids artificial stress gradients across the height, allowing the bimaterial patch test to admit a constant stress solution.

The porous medium is discretized using two quadrilateral parent elements with bilinear shape functions, shown in white and gray in Fig. 21b. Each quadrilateral element is divided by an interface (shown in red) into one triangular and one pentagonal subdomain, which are discretized using four triangular integration elements per quadrilateral element, see Figs. 21c and 21d. Numerical simulations are performed for two cases: (i) *linear* enrichment using 3-node integration elements, depicted in Fig. 21c, and (ii) *quadratic* enrichment using 6-node integration elements, shown in Fig. 21d. Black and red solid circles denote standard and enriched nodes, respectively. As shown in Fig. 21d, in the quadratic enrichment formulation, additional enriched nodes are placed at the centers of the integration element edges.

Figs. 22a and 22b present the resulting normal stress σ_{yy} in the y-direction for the linear and quadratic enrichment cases, respectively, while Figs. 22c and 22d show the corresponding flux q_y in the y-direction. The stress and flux are evaluated at $t = 2.8$ s. When quadrilateral parent elements are subdivided into triangular and pentagonal subdomains, the linear enrichment formulation (Fig. 21c) fails the patch test. This is because the linear enrichment functions do not

include the bilinear term present in the shape functions of the quadrilateral parent elements. In contrast, the quadratic enrichment formulation (Fig. 21d) successfully reproduces the behavior of the 4-node quadrilateral parent elements. Specifically, as shown in Figs. 22b and 22d, the normal stress σ_{yy} and the flux q_y remain uniform across the domain, confirming that the element formulation with the quadratic enrichment passes the patch test.

Data availability

Data will be made available on request.

References

Aragón, A.M., Duarte, A.C., 2023. Fundamentals of Enriched Finite Element Methods. Elsevier-Health Science.

Aragón, A.M., Duarte, C.A., Geubelle, P.H., 2010. Generalized finite element enrichment functions for discontinuous gradient fields. Internat. J. Numer. Methods Engrg. 82 (2), 242–268.

Aragón, A.M., Liang, B., Ahmadian, H., Soghrati, S., 2020. On the stability and interpolating properties of the hierarchical interface-enriched finite element method. Comput. Methods Appl. Mech. Engrg. 362, 112671.

Aragón, A.M., Simone, A., 2017. The discontinuity-enriched finite element method. Internat. J. Numer. Methods Engrg. 112 (11), 1589–1613.

Aragón, A.M., Soghrati, S., Geubelle, P.H., 2013. Effect of in-plane deformation on the cohesive failure of heterogeneous adhesives. J. Mech. Phys. Solids 61 (7), 1600–1611.

Bathe, K.J., 1982. Finite Element Procedures in Engineering Analysis. Prentice Hall, New Jersey.

Belytschko, T., Black, T., 1999. Elastic crack growth in finite elements with minimal remeshing. Internat. J. Numer. Methods Engrg. 45 (5), 601–620.

Biot, M.A., 1941. General theory of three-dimensional consolidation. J. Appl. Phys. 12 (2), 155–164.

Biot, M.A., 1956. Theory of propagation of elastic waves in a fluid-saturated porous solid. II. Higher frequency range. J. Acoust. Soc. Am. 28 (2), 179–191.

Biot, M.A., 1962. Mechanics of deformation and acoustic propagation in porous media. J. Appl. Phys. 33 (4), 1482–1498.

Bowen, R.M., 1980. Incompressible porous media models by use of the theory of mixtures. Internat. J. Engrg. Sci. 18 (9), 1129–1148.

Bowen, R.M., 1982. Compressible porous media models by use of the theory of mixtures. Internat. J. Engrg. Sci. 20 (6), 697–735.

Callari, C., Armero, F., Abati, A., 2010. Strong discontinuities in partially saturated poroplastic solids. Comput. Methods Appl. Mech. Engrg. 199 (23–24), 1513–1535.

Carrier, B., Granet, S., 2012. Numerical modeling of hydraulic fracture problem in permeable medium using cohesive zone model. Eng. Fract. Mech. 79, 312–328.

Cuba-Ramos, A., Aragón, A.M., Soghrati, S., Geubelle, P.H., Molinari, J.F., 2015. A new formulation for imposing Dirichlet boundary conditions on non-matching meshes. Internat. J. Numer. Methods Engrg. 103 (6), 430–444.

Daux, C., Moës, N., Dolbow, J., Sukumar, N., Belytschko, T., 2000. Arbitrary branched and intersecting cracks with the extended finite element method. Internat. J. Numer. Methods Engrg. 48 (12), 1741–1760.

De Boer, R., 2012. Theory of Porous Media: Highlights in Historical Development and Current State. Springer Science & Business Media.

de Borst, R., 2017a. Computational Methods for Fracture in Porous Media: Isogeometric and Extended Finite Element Methods. Elsevier.

de Borst, R., 2017b. Fluid flow in fractured and fracturing porous media: A unified view. Mech. Res. Commun. 80, 47–57.

De Lazzari, E., van den Boom, S.J., Zhang, J., van Keulen, F., Aragón, A.M., 2021. A critical view on the use of Non-Uniform Rational B-Splines to improve geometry representation in enriched finite element methods. Internat. J. Numer. Methods Engrg. 122 (5), 1195–1216.

Fries, T.P., Belytschko, T., 2010. The extended/generalized finite element method: An overview of the method and its applications. Internat. J. Numer. Methods Engrg. 84 (3), 253–304.

Gordeliy, E., Peirce, A., 2013a. Coupling schemes for modeling hydraulic fracture propagation using the XFEM. Comput. Methods Appl. Mech. Engrg. 253, 305–322.

Gordeliy, E., Peirce, A., 2013b. Implicit level set schemes for modeling hydraulic fractures using the XFEM. Comput. Methods Appl. Mech. Engrg. 266, 125–143.

Green, A.E., Naghdi, P.M., 1969. On basic equations for mixtures. Quart. J. Mech. Appl. Math. 22 (4), 427–438.

Hajiabadi, M.R., Khoei, A.R., 2019. A bridge between dual porosity and multiscale models of heterogeneous deformable porous media. Int. J. Numer. Anal. Methods Geomech. 43 (1), 212–238.

Haslinger, J., Renard, Y., 2009. A new fictitious domain approach inspired by the extended finite element method. SIAM J. Numer. Anal. 47 (2), 1474–1499.

Hassanizadeh, M., Gray, W.G., 1980. General conservation equations for multi-phase systems: 3. constitutive theory for porous media flow. Adv. Water Resour. 3 (1), 25–40.

Hassanizadeh, S.M., Gray, W.G., 1990. Mechanics and thermodynamics of multiphase flow in porous media including interphase boundaries. Adv. Water Resour. 13 (4), 169–186.

Hoteit, H., Firoozabadi, A., 2008. Numerical modeling of two-phase flow in heterogeneous permeable media with different capillarity pressures. Adv. Water Resour. 31 (1), 56–73.

Hughes, T.J.R., 1987. The Finite Element Method - Linear Static and Dynamic Finite Element Analyses. Prentice Hall, New Jersey.

Iranmanesh, M.A., Pak, A., 2018. Extrinsically enriched element free Galerkin method for heat and fluid flow in deformable porous media involving weak and strong discontinuities. Comput. Geotech. 103, 179–192.

Iranmanesh, M.A., Pak, A., 2023. Three-dimensional numerical simulation of hydraulically driven cohesive fracture propagation in deformable reservoir rock using enriched EFG method. Comput. Geosci. 27 (2), 317–335.

Irzal, F., Remmers, J.J.C., Huyghe, J.M., de Borst, R., 2013. A large deformation formulation for fluid flow in a progressively fracturing porous material. Comput. Methods Appl. Mech. Engrg. 256, 29–37.

Karimi-Fard, M., Firoozabadi, A., 2001. Numerical simulation of water injection in 2D fractured media using discrete-fracture model. In: SPE Annual Technical Conference and Exhibition. p. 71615.

Kergrene, K., Babuška, I., Banerjee, U., 2016. Stable generalized finite element method and associated iterative schemes; application to interface problems. Comput. Methods Appl. Mech. Engrg. 305, 1–36.

Khoei, A.R., 2014. Extended Finite Element Method: Theory and Applications. John Wiley & Sons.

Khoei, A.R., Amini, D., Mortazavi, S.M.S., 2021. Modeling non-isothermal two-phase fluid flow with phase change in deformable fractured porous media using extended finite element method. Internat. J. Numer. Methods Engrg. 122 (16), 4378–4426.

Khoei, A.R., Barani, O.R., Mofid, M., 2011. Modeling of dynamic cohesive fracture propagation in porous saturated media. Int. J. Numer. Anal. Methods Geomech. 35 (10), 1160–1184.

Khoei, A.R., Haghighat, E., 2011. Extended finite element modeling of deformable porous media with arbitrary interfaces. Appl. Math. Model. 35 (11), 5426–5441.

Khoei, A.R., Moallemi, S., Haghighat, E., 2012. Thermo-hydro-mechanical modeling of impermeable discontinuity in saturated porous media with X-FEM technique. Eng. Fract. Mech. 96, 701–723.

Khoei, A.R., Mohammadnejad, T., 2011. Numerical modeling of multiphase fluid flow in deforming porous media: A comparison between two-and three-phase models for seismic analysis of earth and rockfill dams. Comput. Geotech. 38 (2), 142–166.

Khoei, A.R., Mortazavi, S.M.S., 2020. Thermo-hydro-mechanical modeling of fracturing porous media with two-phase fluid flow using X-FEM technique. Int. J. Numer. Anal. Methods Geomech. 44 (18), 2430–2472.

Khoei, A.R., Saeedmonir, S., 2021. Computational homogenization of fully coupled multiphase flow in deformable porous media. Comput. Methods Appl. Mech. Engrg. 376, 113660.

Khoei, A.R., Saeedmonir, S., Bonabi, A.M., 2023a. Computational homogenization of fully coupled hydro-mechanical analysis of micro-fractured porous media. Comput. Geotech. 154, 105121.

Khoei, A.R., Saeedmonir, S., Hosseini, N., Mousavi, S.M., 2023b. An X-FEM technique for numerical simulation of variable-density flow in fractured porous media. MethodsX 10, 102137.

Khoei, A., Vahab, M., Hirmand, M., 2018. An enriched–FEM technique for numerical simulation of interacting discontinuities in naturally fractured porous media. Comput. Methods Appl. Mech. Engrg. 331, 197–231.

Li, C., Borja, R.I., Regueiro, R.A., 2004. Dynamics of porous media at finite strain. Comput. Methods Appl. Mech. Engrg. 193 (36–38), 3837–3870.

Li, T., Han, D., Yang, F., Li, J., Wang, D., Yu, B., Wei, J., 2021. Modeling study of the thermal-hydraulic-mechanical coupling process for EGS based on the framework of EDFM and XFEM. Geothermics 89, 101953.

Liu, D., van den Boom, S.J., Simone, A., Aragón, A.M., 2022. An interface-enriched generalized finite element formulation for locking-free coupling of non-conforming discretizations and contact. Comput. Mech. 70 (3), 477–499.

Liu, D., Zhang, J., Aragón, A.M., Simone, A., 2025. The discontinuity-enriched finite element method for multiple intersecting discontinuities. Comput. Methods Appl. Mech. Engrg. 433, 117432.

Lotfian, Z., Sivaselvan, M.V., 2018. Mixed finite element formulation for dynamics of porous media. Internat. J. Numer. Methods Engrg. 115 (2), 141–171.

Moës, N., Dolbow, J., Belytschko, T., 1999. A finite element method for crack growth without remeshing. Internat. J. Numer. Methods Engrg. 46 (1), 131–150.

Mohammadnejad, T., Andrade, J.E., 2016. Numerical modeling of hydraulic fracture propagation, closure and reopening using XFEM with application to in-situ stress estimation. Int. J. Numer. Anal. Methods Geomech. 40 (15), 2033–2060.

Mohammadnejad, T., Khoei, A.R., 2013a. An extended finite element method for fluid flow in partially saturated porous media with weak discontinuities; the convergence analysis of local enrichment strategies. Comput. Mech. 51, 327–345.

Mohammadnejad, T., Khoei, A.R., 2013b. An extended finite element method for hydraulic fracture propagation in deformable porous media with the cohesive crack model. Finite Elem. Anal. Des. 73, 77–95.

Mohammadnejad, T., Khoei, A.R., 2013c. Hydro-mechanical modeling of cohesive crack propagation in multiphase porous media using the extended finite element method. Int. J. Numer. Anal. Methods Geomech. 37 (10), 1247–1279.
Monteagudo, J.E.P., Firoozabadi, A., 2004. Control-volume method for numerical simulation of two-phase immiscible flow in two-and three-dimensional discrete-fractured media. Water Resour. Res. 40 (7).
Mortazavi, S.M.S., Beydokhti, O.R., Khoei, A.R., 2023. Modeling enhanced geothermal systems using a hybrid XFEM–ECM technique. Appl. Therm. Eng. 230, 120755.
Mortazavi, S.M.S., Khoei, A.R., 2024. Coupled thermo-hydro-mechanical and chemical (THMC) simulation of silicate rocks with an enriched–FEM model. Comput. Geotech. 173, 106575.
Mortazavi, S.M.S., Pirmoradi, P., Khoei, A.R., 2022. Numerical simulation of cold and hot water injection into naturally fractured porous media using the extended–FEM and an equivalent continuum model. Int. J. Numer. Anal. Methods Geomech. 46 (3), 617–655.
Newmark, N.M., 1959. A method of computation for structural dynamics. J. Eng. Mech. Div. 85 (3), 67–94.
Noble, D.R., Newren, E.P., Lechman, J.B., 2010. A conformal decomposition finite element method for modeling stationary fluid interface problems. Internat. J. Numer. Methods Fluids 63 (6), 725–742.
Prévost, J.H., 1980. Mechanics of continuous porous media. Internat. J. Engrg. Sci. 18 (6), 787–800.
Prevost, J.H., 1982. Nonlinear transient phenomena in saturated porous media. Comput. Methods Appl. Mech. Engrg. 30 (1), 3–18.
Qin, X., Han, D.-H., Zhao, L., 2022. Measurement of grain bulk modulus on sandstone samples from the norwegian continental shelf. J. Geophys. Res.: Solid Earth 127 (9), e2022JB024550.
Remij, E.W., Remmers, J.J.C., Huyghe, J.M., Smeulders, D.M.J., 2015. The enhanced local pressure model for the accurate analysis of fluid pressure driven fracture in porous materials. Comput. Methods Appl. Mech. Engrg. 286, 293–312.
Réthoré, J., de Borst, R., Abellan, M.A., 2007. A two-scale approach for fluid flow in fractured porous media. Internat. J. Numer. Methods Engrg. 71 (7), 780–800.
Réthoré, J., de Borst, R., Abellan, M.A., 2008. A two-scale model for fluid flow in an unsaturated porous medium with cohesive cracks. Comput. Mech. 42, 227–238.
Sarris, E., Papanastasiou, P., 2012. Modeling of hydraulic fracturing in a poroelastic cohesive formation. Int. J. Geomech. 12 (2), 160–167.
Scheperboer, I.C., Suiker, A.S.J., Bosco, E., Clemens, F.H.L.R., 2022. A coupled hydro-mechanical model for subsurface erosion with analyses of soil piping and void formation. Acta Geotech. 17, 4769–4798.
Schrefler, B.A., Scotta, R., 2001. A fully coupled dynamic model for two-phase fluid flow in deformable porous media. Comput. Methods Appl. Mech. Engrg. 190 (24–25), 3223–3246.
Schrefler, B.A., Xiaoyong, Z., 1993. A fully coupled model for water flow and airflow in deformable porous media. Water Resour. Res. 29 (1), 155–167.
Schrefler, B.A., Zhang, H.W., Pastor, M., Zienkiewicz, O.C., 1998. Strain localisation modelling and pore pressure in saturated sand samples. Comput. Mech. 22 (3), 266–280.
Secchi, S., Simoni, L., Schrefler, B.A., 2007. Mesh adaptation and transfer schemes for discrete fracture propagation in porous materials. Int. J. Numer. Anal. Methods Geomech. 31 (2), 331–345.
Segura, J.M., Carol, I., 2008. Coupled HM analysis using zero-thickness interface elements with double nodes. Part I: Theoretical model. Int. J. Numer. Anal. Methods Geomech. 32 (18), 2083–2101.
Sheng, D., Gens, A., Fredlund, D.G., Sloan, S.W., 2008. Unsaturated soils: from constitutive modelling to numerical algorithms. Comput. Geotech. 35 (6), 810–824.
Sheng, D., Sloan, S.W., Gens, A., Smith, D.W., 2003. Finite element formulation and algorithms for unsaturated soils. Part I: Theory. Int. J. Numer. Anal. Methods Geomech. 27 (9), 745–765.
Simoni, L., Secchi, S., 2003. Cohesive fracture mechanics for a multi-phase porous medium. Eng. Comput. 20 (5/6), 675–698.
Soghrati, S., 2014. Hierarchical interface-enriched finite element method: An automated technique for mesh-independent simulations. J. Comput. Phys. 275, 41–52.
Soghrati, S., Aragón, A.M., Duarte, A.C., Geubelle, P.H., 2012. An interface-enriched generalized FEM for problems with discontinuous gradient fields. Internat. J. Numer. Methods Engrg. 89 (8), 991–1008.
Truesdell, C., Toupin, R., 1960. The Classical Field Theories. Springer, Berlin.
van Bergen, S., Norte, R.A., Aragón, A.M., 2024. An interface-enriched generalized finite element method for the analysis and topology optimization of 2-D electromagnetic problems. Comput. Methods Appl. Mech. Engrg. 421, 116748.
van den Boom, S.J., Abedi, R., van Keulen, F., Aragón, A.M., 2023. A level set-based interface-enriched topology optimization for the design of phononic crystals with smooth boundaries. Comput. Methods Appl. Mech. Engrg. 408, 115888.
van den Boom, S.J., Zhang, J., van Keulen, F., Aragón, A.M., 2019. A stable interface-enriched formulation for immersed domains with strong enforcement of essential boundary conditions. Internat. J. Numer. Methods Engrg. 120 (10), 1163–1183.
van den Boom, S.J., Zhang, J., van Keulen, F., Aragón, A.M., 2021. An interface-enriched generalized finite element method for level set-based topology optimization. Struct. Multidiscip. Optim. 63 (1), 1–20.
Varnosfaderani, A.M., Gatmiri, B., Haghighi, E.M., 2017. A model for moisture and heat flow in fractured unsaturated porous media. Int. J. Numer. Anal. Methods Geomech. 41 (6), 828–858.
Wang, W., Kosakowski, G., Kolditz, O., 2009. A parallel finite element scheme for thermo-hydro-mechanical (THM) coupled problems in porous media. Comput. Geosci. 35 (8), 1631–1641.
Whitaker, S., 1977. Simultaneous heat, mass, and momentum transfer in porous media: a theory of drying. Adv. Heat Transf. 13, 119–203.
Zhang, Q., Banerjee, U., Babuška, I., 2020. Strongly stable generalized finite element method (SSGFEM) for a non-smooth interface problem II: A simplified algorithm. Comput. Methods Appl. Mech. Engrg. 363, 112926.
Zhang, J., van den Boom, S.J., van Keulen, F., Aragón, A.M., 2019. A stable discontinuity-enriched finite element method for 3-D problems containing weak and strong discontinuities. Comput. Methods Appl. Mech. Engrg. 355, 1097–1123.
Zhang, H.W., Fu, Z.D., Wu, J.K., 2009. Coupling multiscale finite element method for consolidation analysis of heterogeneous saturated porous media. Adv. Water Resour. 32 (2), 268–279.
Zhang, J., van Keulen, F., Aragón, A.M., 2022. On tailoring fracture resistance of brittle structures: A level set interface-enriched topology optimization approach. Comput. Methods Appl. Mech. Engrg. 388, 114189.
Zhang, J., Yan, Y., Duarte, A.C., Aragón, A.M., 2025. A discontinuity-enriched finite element method for modeling quasi-static fracture in brittle solids. Comput. Methods Appl. Mech. Engrg. 435, 117585.
Zienkiewicz, O.C., 1982. Basic formulation of static and dynamic behaviours of soil and other porous media. Appl. Math. Mech. 3 (4), 457–468.
Zienkiewicz, O.C., Chan, A.H.C., Pastor, M., Paul, D.K., Shiomi, T., 1990a. Static and dynamic behaviour of soils: a rational approach to quantitative solutions. I. Fully saturated problems. Proc. R. Soc. A 429 (1877), 285–309.
Zienkiewicz, O.C., Chan, A.H.C., Pastor, M., Schrefler, B.A., Shiomi, T., 1999. Computational Geomechanics. John Wiley and Sons, Chichester, England.
Zienkiewicz, O.C., Chang, C.T., Bettess, P., 1980. Drained, undrained, consolidating and dynamic behaviour assumptions in soils. Geotechnique 30 (4), 385–395.
Zienkiewicz, O.C., Xie, Y.M., Schrefler, B.A., Ledesma, A., Bičanič, N., 1990b. Static and dynamic behaviour of soils: a rational approach to quantitative solutions. II. Semi-saturated problems. Proc. R. Soc. A 429 (1877), 311–321.